Journal of Materials Chemistry B

PAPER

Plasmonic hot-electron-assisted ultra-stretchable hydrogel electrodes for wearable cardiovascular monitoring and AI-driven predictive analytics

Bangul Khan, [iD] [ab] Syed Bilal Ahmed,[c] Bilawal Khan,[d] Muhammad Shehzad Khan,[b] Liangyi Lyu,[be] Iyappan Gunasekaran,[b] Rafi u Shan Ahmad,[ab] Junchen Liao,[a] Mohamed Elhousseini Hilal*[a] and Bee Luan Khoo [iD] *[abf]

Wearable bioelectronic systems require soft, deformable materials that maintain high electrical conductivity and reliable interfacial charge transport under large mechanical strains. However, most existing hydrogel- or elastomer-based conductors involve trade-offs among mechanical compliance, electrical performance, and long-term biocompatibility, making it challenging to integrate all three properties within a single material platform. Here, we introduce a plasmonic hot-electron-assisted conductive PAM−PEDOT:PSS−Ag hydrogel, engineered to address these multifunctional requirements for continuous cardiovascular monitoring. Silver nanoparticles (Ag NPs) dispersed within the hydrogel matrix generate localised surface plasmon resonance (LSPR) under UV irradiation, producing smooth, spatially uniform heating and hot-electron injection throughout the precursor solution. This synergistic plasmonic heating effect accelerates polymerisation ($\sim$420 s; 0.1167 h), enhances network homogeneity, and lowers interfacial charge-transfer resistance by promoting more ordered PEDOT:PSS chain assembly and improved crosslinking dynamics. As a result, the hydrogel exhibits ultrahigh stretchability ($>$2000%), stable conductivity ($\sim$328.82 $\pm$ 1.78 mS m^{-1}), and intrinsic antibacterial activity ($\geq$99.7%). The material exhibits consistent electromechanical performance from -20 °C to 40 °C, showing tunable strain sensitivity governed by temperature-dependent network mechanics and ionic mobility. When used as epidermal electrodes, the hydrogel enables high-fidelity electrocardiogram (ECG) acquisition (SNR $\approx$ 25 dB) in human and rodent models. Integrated with machine-learning analytics, the platform supports accurate demographic prediction (96.2%), demonstrating a scalable material-device-data framework for next-generation personalised cardiovascular monitoring.

1. Introduction

Cardiovascular diseases (CVDs) remain the leading cause of mortality worldwide, responsible for approximately 17.9 million deaths annually. Conditions such as hypertension, coronary artery disease, and myocardial infarction continue to pose significant global health challenges due to their chronic progression and the substantial burden they place on healthcare systems. Continuous and accurate monitoring is therefore essential for early diagnosis, timely clinical intervention, and the prevention of adverse outcomes.[1–3]

Electrocardiography (ECG), which captures the heart's electrical activity, is a potent modality for detecting cardiac abnormalities and enabling long-term physiological assessment.[4] However, conventional ECG systems rely on rigid, bulky, clinic-based instrumentation, restricting their accessibility and limiting their ability to provide continuous, real-world monitoring.[5]

Wearable ECG technologies offer a promising alternative by enabling real-time, non-invasive acquisition of electrophysiological signals.[6] To date, substrates such as polydimethylsiloxane (PDMS),[7] polyimide (PI),[8] and various textiles,[9] combined with conductive fillers including carbon nanomaterials, gold nanomaterials, and 2D nanomaterials, have been extensively investigated for wearable ECG applications.[10] Despite these advancements, many of these materials still suffer from

[a] Department of Biomedical Engineering, College of Biomedicine, City University of Hong Kong, Tat Chee Ave, Kowloon, Hong Kong SAR. E-mail: blkhoo@cityu.edu.hk, melhouss@um.city.edu.hk

[b] Hongkong Centre of Cerebro-Cardiovascular Health Engineering (COCHE), Shatin, Hong Kong

[c] School of Science, Harbin Institute of Technology (Shenzhen), Shenzhen 518055, China

[d] Department of Materials Science and Engineering, City University of Hong Kong, Tat Chee Ave, Kowloon, Hong Kong SAR

[e] Department of Electrical Engineering, City University of Hong Kong, Tat Chee Ave, Kowloon, Hong Kong SAR

[f] Institute of Digital Medicine, City University of Hong Kong, Hong Kong, SAR 999077, P. R. China

5408 | *J. Mater. Chem. B*, 2026, **14**, 5408–5427

This journal is © The Royal Society of Chemistry 2026

inadequate skin conformity, limited biocompatibility, mechanical rigidity, and weak adhesion. These factors increase contact impedance and exacerbate motion artefacts during electrophysiological recordings.[11–13]

Hydrogels, three-dimensional hydrophilic polymer networks with high water content, intrinsic stretchability, biocompatibility, and mixed ionic/electronic conductivity, have emerged as promising candidates for next-generation wearable ECG interfaces.[14,15] Although traditional conductive materials offer excellent electrical performance, they often raise concerns of immunogenicity or cytotoxicity when integrated into soft biological environments.[16] Conductive polymer-based hydrogels, such as polypyrrole, polyaniline, and PEDOT:PSS, can enhance conductivity but typically compromise extreme deformability and long-term mechanical resilience.[17,18] As a result, the long-standing bioelectronic compatibility paradox persists, reflecting the inherent difficulty of simultaneously reconciling the mechanical softness required by biological tissues with the electronic performance demanded by sensing devices.[19,20]

This mismatch is further amplified by the fact that human skin is soft, viscoelastic, and susceptible to bacterial colonisation during prolonged monitoring. In contrast, conventional electronic materials rely on rigid crystalline frameworks with limited stretchability and low charge-transport efficiency. These disparities collectively form a mechanical–electrical–biological trilemma in which optimising one functional domain often degrades another, thereby limiting the reliability and long-term stability of wearable electrophysiological interfaces.[21]

Beyond material limitations, existing cardiovascular monitoring systems frequently lack adaptability and intelligent analytics capabilities for real-world physiological environments. Traditional platforms are not inherently equipped to interpret complex biosignals or provide predictive insights. Integrating artificial intelligence (AI) into wearable bioelectronic systems offers a transformative pathway to address these limitations. AI-enabled algorithms can enhance signal conditioning, suppress motion artefacts, and support real-time interpretation of ECG waveforms, elevating wearable devices from passive diagnostic tools to proactive, innovative health-assessment platforms.[22–24]

We present a multifunctional, plasmonically enhanced conductive hydrogel (PAM–PEDOT:PSS–Ag) that meets the competing requirements of ultra-stretchability, high electrical conductivity, and biocompatibility for wearable bioelectronic interfaces. In this system, Ag NPs were embedded within a PEDOT:PSS–PAM network to generate hot electrons via localised surface plasmon resonance (LSPR) under UV excitation. The resulting uniform spatially smooth heating and hot-electron injection facilitate more efficient charge transport while preserving the hydrogel's intrinsic softness and extreme deformability. A spatially smooth heating-based polymerisation strategy enables rapid gelation within 420 s and supports scalable fabrication with consistent mechanical and electrical characteristics. When applied as epidermal electrodes, the hydrogel delivers stable, high-fidelity ECG recordings in both human and rodent models, achieving an SNR of approximately 25 dB. Coupled with machine-learning algorithms, the system achieves 96.2% predictive accuracy in demographic prediction, highlighting its potential as an intelligent, biocompatible platform for continuous cardiovascular monitoring and next-generation wearable bioelectronics.

2. Results and discussion

2.1. Molecular analysis of plasmon-driven hot electron dynamics mediating PAM–PEDOT:PSS–Ag hydrogels

This section describes the methodology, followed by the non-covalent interaction (NCI) analysis to understand intermolecular and weak molecular interactions in the complex hydrogel system.

A schematic of the methodology is presented in Fig. 1A, in which Ag-NPs were ultrasonicated in an aqueous solution containing PEDOT:PSS to prevent agglomeration. This was followed by the sequential addition of acrylamide (AM), NN'-methylenebisacrylamide (MBAA), ammonium persulfate (APS), and glycerol in exact amounts as specified in the desired hydrogel formulation (Table S1, SI). Focused UV irradiation was then used to exploit the plasmonic effect of Ag-NPs, generating localised spatial smooth heating and injecting hot electrons into PEDOT:PSS to stimulate uniform crosslinking of the hydrogel. A highly stretchable hydrogel with superior electrical conductivity was realised within 420 s.

The molecular mechanistic interactions and compatibility among the components of the hydrogel composite were elucidated via detailed NCI analysis via density functional theory (DFT) and the Multiwfn simulation environment.[25,26] The study was carried out on PAM, PEDOT:PSS, glycerol, PEDOT:PSS–Ag, PAM–PEDOT:PSS–glycerol, and PAM–PEDOT:PSS–Ag–glycerol hydrogels to illuminate the crucial role played by intermolecular forces and weak molecular interactions in the synthesis and performance of a highly stretchable plasmon-driven hydrogel, developed for AI-enhanced cardiovascular health monitoring.

Fig. S1(A–C) illustrates the optimised molecular structure of PAM, the corresponding NCI simulation, and the RDG plot. It is well known that PAM has a dense network of hydrogen bonds between the amide groups,[27] which in RDG plots translates into concentrated blue regions in the range $0.02 < |\text{sign}(\lambda_2)\rho| < 0.04$, corresponding to strong, attractive interactions between the carbonyl oxygen and amide hydrogen atoms. These interactions result in a coherent, stretchable polymer matrix in which mechanical flexibility and water retention are balanced to enable conducting hydrogel systems.[28]

Glycerol is widely preferred in the soft hydrogel system because it helps the polymeric matrix maintain structural integrity over long periods. The NCI RDG analysis of glycerol was conducted to assess hydrogen bonding, as illustrated in Fig. S2(A–C). The results demonstrated stronger hydrogen bonding due to the presence of hydroxyl groups, which act as plasticisers, preventing brittleness and fractures.[29]

Fig. 1B(I–III) shows the optimised structure of PEDOT: PSS, along with its NCI and RDG plots, illustrating various

This journal is © The Royal Society of Chemistry 2026

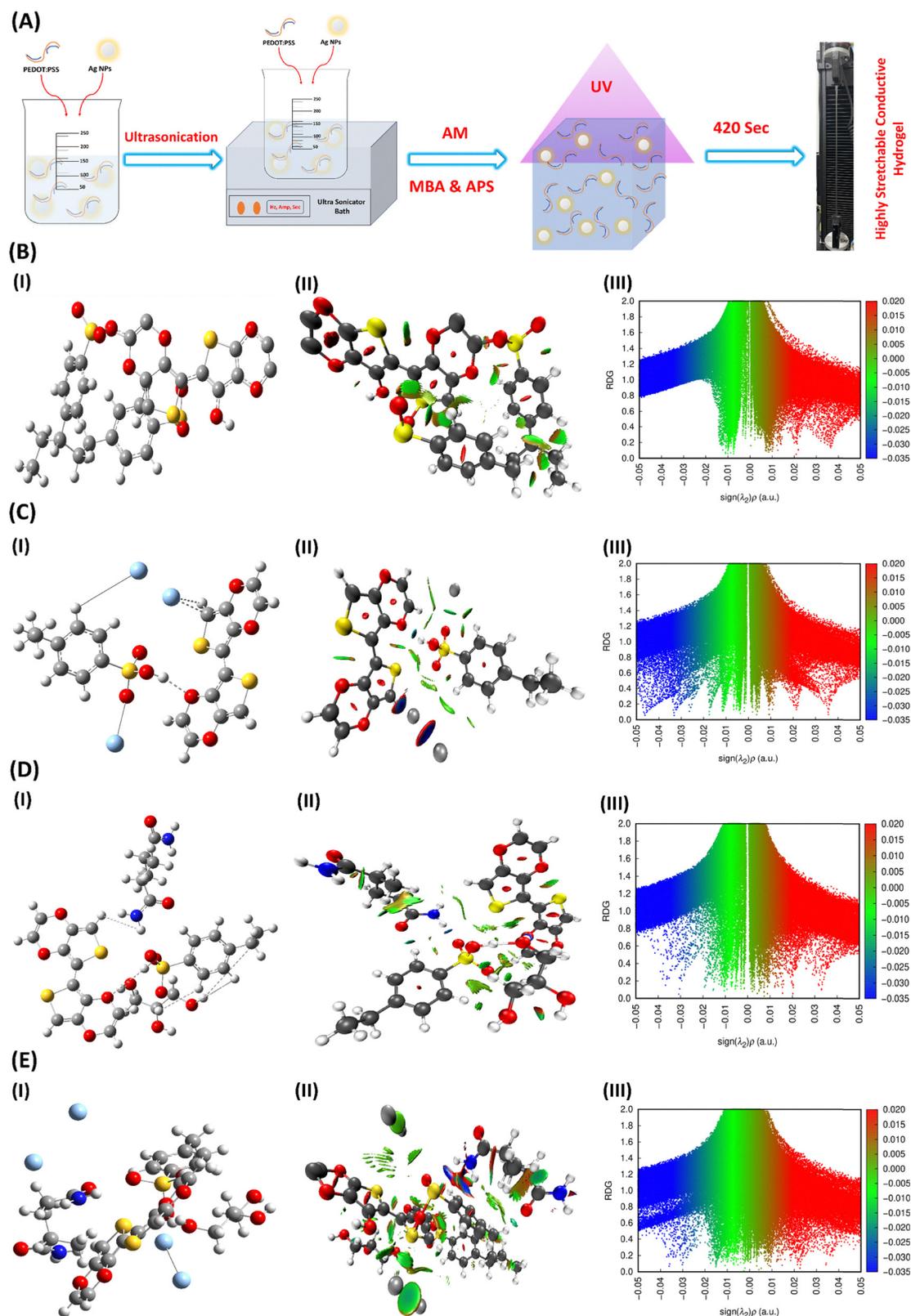*J. Mater. Chem. B*, 2026, **14**, 5408–5427 | **5409**

Fig. 1 Methodology and NCI analysis of plasmon-driven hot electron dynamics mediating PAM–PEDOT:PSS–Ag hydrogel. (A) Synthesis scheme of the plasmon-driven hot electron dynamics mediating the PAM–PEDOT:PSS–Ag hydrogel. (B) Non-covalent interaction analysis of PEDOT:PSS. (I) Optimised molecular structure of PEDOT:PSS, (II) NCI simulated molecular structure of PEDOT:PSS, and (III) RDG plot of PEDOT:PSS. (C) Non-covalent interaction analysis of PEDOT:PSS–Ag NPs. (I) Optimized structure of PEDOT:PSS–Ag NPs, (II) NCI of the optimized structure of PEDOT:PSS–Ag NPs, and (III) RDG plot of the PEDOT:PSS–Ag NPs. (D) Non-covalent interaction analysis of PAM–PEDOT:PSS–glycerol. (I) Optimized structure of PAM–PEDOT:PSS–glycerol, (II) NCI of the optimized structure of PAM–PEDOT:PSS–glycerol, and (III) RDG plot of PAM–PEDOT:PSS–glycerol. (E) Non-covalent interaction analysis of PAM–PEDOT:PSS–glycerol–Ag NPs. (I) Optimized structure of PAM–PEDOT:PSS–glycerol–Ag NPs, (II) NCI of the optimized structure of PAM–PEDOT:PSS–glycerol–Ag NPs, and (III) RDG plot of the PAM–PEDOT:PSS–glycerol–Ag NPs.

5410 | J. Mater. Chem. B, 2026, 14, 5408–5427

This journal is © The Royal Society of Chemistry 2026

interactions, such as π–π stacking of the conjugated PEDOT chains and hydrogen bonding between the sulfonate groups of PSS.[30] The higher blue (attractive) and green (van der Waals) domains reveal distinct intermolecular forces, which are crucial for the polymer's electronic conductivity without compromising its structural integrity.[31] A new dimension of interaction was introduced by Ag NPs when they were doped with the PEDOT:PSS system, as depicted in Fig. 1C(I). The NCI plot, Fig. 1C(II), and the RDG plots, Fig. 1C(III), of Ag–PEDOT:PSS exhibit new blue regions corresponding to silver–sulfur and silver–oxygen coordination interactions. These interactions are of prime importance for Ag NPs' antibacterial activity, enabling them to be in close contact with their polymer chains.[32,33]

Fig. 1D(I) shows the optimised molecular structure of the PAM–PEDOT:PSS–glycerol complex without Ag-NPs. Fig. 1D(II and III) depicts the interaction by NCI and its RDG plots, demonstrating manifold regions of hydrogen bonding and van der Waals forces contributed from the PAM matrix,[34] while π–π stacking from PEDOT:PSS.[35] More interestingly, glycerol acts as an intermediary between the hydrophilic PAM and the hydrophobic PEDOT:PSS domains, helping ensure homogeneous distribution and maintaining the matrix's mechanical flexibility and electrical conductivity.[36]

Fig. 1E(I–III) illustrates the optimised molecular structure of a PAM–PEDOT:PSS–glycerol–Ag NP hydrogel system, along with NCI-RDG plots, showing a robust interaction network with increased blue regions due to strong attraction and hydrogen bonding from glycerol and PEDOT:PSS.[37] In contrast, an enhanced green region (van der Waals interaction) indicates additional stabilisation of the PAM polymeric matrix induced by Ag NPs.[38] Furthermore, there is also a strong repulsion and steric effect (red region) in the hydrogel system due to the physical disturbance of PEDOT:PSS interactions, altering PEDOT's conformation toward a more conductive form because of Ag NPs, which contribute to localized field enhancements that improve charge transfer between Ag and the PEDOT chain. Moreover, Fig. S3 illustrates the colour codes for elements used in molecular structures and the RDG plots' reference colour bar.

The NCI analyses suggest that the materials in the PAM–PEDOT:PSS–glycerol–Ag NP hydrogel system interact compatibly at the molecular level. These weak molecular forces, combined with Ag NPs' plasmonic properties, significantly enhance mechanical, electrical, and antibacterial properties, which are crucial for long-term cardiovascular monitoring.

2.2. Materials characterization of plasmon-driven hot electron dynamics mediating PAM–PEDOT:PSS–Ag hydrogels

This section presents a comprehensive characterisation of a PAM–PEDOT:PSS–Ag hydrogel system, with emphasis on its plasmon-driven hot-electron dynamics. A suite of analytical techniques, including X-ray photoelectron spectroscopy (XPS), Fourier transform infrared spectroscopy (FTIR), scanning electron microscopy (SEM) with energy-dispersive X-ray spectroscopy (EDS) and thermogravimetric analysis (TGA), were employed to characterise in detail the chemical composition, molecular interactions, morphological features, and thermal stability of the PAM–PEDOT:PSS–Ag hydrogel composite.

XPS was used to identify the electronic structure, chemical composition, and bonding states of PAM, PAM–1% PEDOT:PSS, and PAM–1% PEDOT:PSS–10% Ag hydrogels to elucidate the role of plasmon-driven hot-electron dynamics in hydrogel gelation, thereby enhancing stretchability for physiological monitoring.

Fig. S4 illustrates the XPS survey spectra of the pure PAM hydrogel (black_graph), demonstrating the presence of C1s, N1s, and O1s elements, while upon the doping of PEDOT:PSS, the XPS survey (red_graph) retains all the core elements of PAM with additional S2p peaks, confirming the successful doping of PEDOT:PSS in the PAM matrix. The incorporation of Ag NPs in the PAM–PEDOT:PSS hydrogel is reflected in (blue_graph), with the additional peak of Ag3d corresponding to silver nanoparticles and confirmation of the successful synthesis of the plasmon-driven hot electron dynamics-mediated PAM–PEDOT:PSS–Ag hydrogel.

Moreover, the high-resolution C1s spectrum of the PAM hydrogel (Fig. S5A) was deconvoluted into three peaks at 284.05 eV, 285.6 eV, and 287.6 eV, corresponding to C–H/C–C, –C–O, and –CONH$_2$ groups, respectively.[39] The N1s spectrum of the PAM hydrogel (Fig. S5B) exhibited peaks at 399.2 eV and 400.3 eV, assigned to N–C and H$_2$N–C bonds.[40,41] The O1s spectrum of the PAM hydrogel (Fig. S5C) displayed two peaks at 531.8 eV and 531.2 eV, which correspond mainly to the C=O group in H$_2$N–C=O.[42]

Upon incorporating 1% PEDOT:PSS to form the PAM–1% PEDOT:PSS hydrogel, the C1s spectrum (Fig. 2A) demonstrated peaks at 283.9 eV, 285.2 eV, and 287.24 eV, attributed to C–H/C–C, –C–O/-C–S, and C=O/-CONH$_2$, respectively.[39,43,44] Compared to the PAM hydrogel, all peaks in the PAM–1% PEDOT:PSS hydrogel shifted to lower binding energy values, which can be attributed to the increased electron density and less electrophilic environment introduced by sulphur in PEDOT:PSS.[45,46] The N1s spectrum of the PAM–1% PEDOT:PSS hydrogel (Fig. 2B) shows peaks at 398.8 eV (N–C) and 401.1 eV (N–H).[14] A shift to lower binding energy for N–C and to higher energy for N–H, compared to the PAM hydrogel, suggests bond weakening and strengthening due to the incorporation of PEDOT:PSS.[45–48] In the O1s spectrum of the PAM–1% PEDOT:PSS hydrogel (Fig. S5D), peaks were observed at 531.1 eV and 532.5 eV, attributed to PSS O=S/O=C and PEDOT C–O–C, respectively.[49] The shift of the O=C peak to lower energy can also be linked to the sulphur-induced increase in electron density and to less electrophilic effects.[45,46] The S2p spectrum of the PAM–1% PEDOT:PSS hydrogel (Fig. 2C) revealed four peaks at 166.9 eV, 167.5 eV, 168.1 eV, and 168.8 eV corresponding to PEDOT (S2p$_{3/2}$, S2p$_{1/2}$) and PSS (S2p$_{3/2}$, S2p$_{1/2}$).[50]

Further incorporation of Ag NPs into the PAM–1% PEDOT: PSS hydrogel composite, forming the PAM–1% PEDOT: PSS–10% Ag hydrogel, resulted in additional spectral changes. The C1s spectrum of the PAM–1% PEDOT:PSS–10% Ag hydrogel (Fig. 2D) displayed peaks at 284.26 eV, 285.61 eV, and 287.47 eV, which were attributed to C–H/C–C, –C–O/-C–S, and C=O/-CONH$_2$, respectively.[39,43,44] All the peaks were shifted to

This journal is © The Royal Society of Chemistry 2026

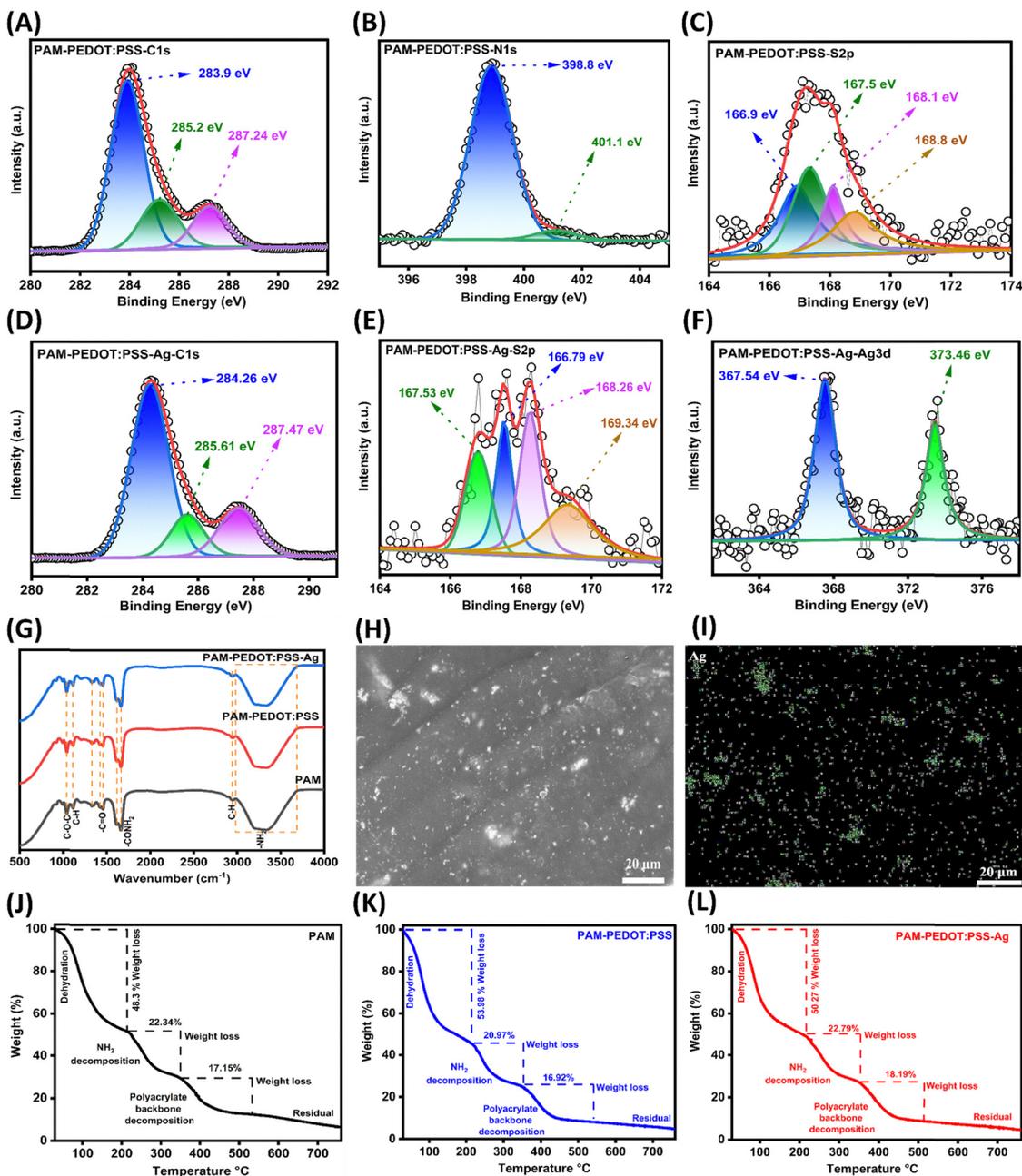*J. Mater. Chem. B*, 2026, **14**, 5408–5427 | **5411**

Fig. 2 Elemental, structural and morphological and thermal characterisation of the PAM, PAM–1% PEDOT:PSS, and PAM–1% PEDOT:PSS–10% Ag hydrogels. (A) XPS deconvolution of the C1s peak of the PAM–1% PEDOT:PSS hydrogel, (B) XPS deconvolution of the N1s peak of the PAM–1% PEDOT:PSS hydrogel, (C) XPS deconvolution of the S2p peak of the PAM–1% PEDOT:PSS hydrogel, (D) XPS deconvolution of the C1s peak of the PAM–1% PEDOT:PSS–10% Ag hydrogel, (E) XPS deconvolution of the S2p peak of the PAM–1% PEDOT:PSS–10% Ag hydrogel, (F) XPS deconvolution of the Ag3d peak of the PAM–1% PEDOT:PSS–10% Ag hydrogel, (G) Fourier Transform Infrared Spectroscopy (FTIR) of the PAM, PAM–1% PEDOT:PSS, and PAM–1% PEDOT:PSS–10% Ag hydrogels, (H) Scanning electron microscopy (SEM) image of the PAM–1% PEDOT:PSS–10% Ag hydrogel, (I) SEM energy-dispersive spectroscopy (EDS) mapping of silver (Ag) in the PAM–1% PEDOT:PSS–10% Ag hydrogel. (J) Thermogravimetric analysis (TGA) graph of the PAM hydrogel, (K) Thermogravimetric analysis (TGA) graph of the PAM–1% PEDOT:PSS hydrogel, and (L) Thermogravimetric analysis (TGA) graph of the PAM–1% PEDOT:PSS–10% Ag hydrogel.

higher binding energies than in the PAM–1% PEDOT:PSS hydrogel, due to silver's diminished electron density and its electrophilic nature.[47,48] In the N1s spectrum of the PAM–1% PEDOT:PSS–10% Ag hydrogel (Fig. S5E), the peaks appeared at 399.24 eV and 400.75 eV for N–C and N–H, respectively.[51] Compared to the PAM–1% PEDOT:PSS hydrogel, the N–C peak

shifted to a higher value, while the N–H peak shifted to a lower value, indicating bond strengthening and weakening due to Ag NPs, the opposite effect of PEDOT:PSS.[45–48]

The XPS spectrum for O1s in the PAM–1% PEDOT:PSS–10% Ag hydrogel (Fig. S5F) reveals peaks at 531.6 eV and 532.5 eV, which were attributed to PSS O=S/Ag–O and PEDOT

5412 | J. Mater. Chem. B, 2026, 14, 5408–5427

This journal is © The Royal Society of Chemistry 2026

C–O–C.[49,52,53] The binding energies of both peaks increased, indicative of bond strengthening in an electrophilic Ag environment.[47,48] Fig. 2E presents the S2p spectra of the PAM–1% PEDOT:PSS–10% Ag hydrogel with four peaks centred at 167.53 eV, 166.79 eV, 168.26 eV, and 169.34 eV, corresponding to PEDOT (S2p$_{3/2}$, S2p$_{1/2}$) and PSS (S2p$_{3/2}$, S2p$_{1/2}$)[50] respectively, with the addition of Ag NPs, the PEDOT S2p$_{1/2}$ and PSS (S2p$_{3/2}$, S2p$_{1/2}$) peaks shifted to higher binding energies, while the PEDOT S2p$_{3/2}$ peak shifted to a lower value. All these changes indicate a specific interaction between Ag NPs and sulphur-containing groups, driven by Ag's electrophilicity.[47,48] The presence of metallic silver in PAM–1% PEDOT:PSS–10% Ag was further confirmed by the Ag3d spectrum, as presented in Fig. 2F, with two peaks at 367.54 and 373.46 eV, corresponding to Ag3d$_{5/2}$ and Ag3d$_{3/2}$,[54] respectively.

FTIR was performed to investigate the structural features and confirm the successful incorporation of Ag NPs and PEDOT:PSS into the PAM polymeric matrix. Fig. 2G shows a peak at 1040 cm^{-1} assigned to the C–O–C stretching vibration, indicative of the polyacrylamide backbone.[55] In contrast, the peak at 1114 cm^{-1} corresponds to the stretching vibration of the C–H bond.[56] A peak at 1457.5 cm^{-1} was assigned to the C=O stretching vibration.[57,58] The peak at 1664.5 cm^{-1} corresponds to the N–H in-plane bending of the –CONH$_2$ group.[59] The band at 2944 cm^{-1} is associated with the asymmetrical stretching of saturated C–H bonds.[55,60] The broad and strong absorption band between 2980 and 3700 cm^{-1}, whose minimum is at 3355 cm^{-1}, is related to –NH$_2$ stretching vibrations.[58,60]

Compared with the PAM–1% PEDOT:PSS hydrogel and PAM–1% PEDOT:PSS–10% Ag hydrogel, all characteristic peaks of PAM were preserved, which proves that the main chain of the polymer did not experience any structural change. More interestingly, the broad band corresponding to the stretching of NH$_2$ (between 2980–3700 cm^{-1}) for pristine PAM narrowed and shifted to 3340 cm^{-1} for both modified samples. It signifies that PEDOT:PSS (red_graph) and PEDOT:PSS–Ag (blue_graph) interacted and were effectively incorporated into the PAM matrix. Since no new peaks appeared, this further demonstrated that no additional functional groups were added, indicating that these components are naturally compatible and mix well.

Fig. 2(H and I) show the SEM-EDS analysis of the plasmon-driven hot electron dynamics mediating PAM–1% PEDOT:PSS–10% Ag hydrogel, revealing a porous hydrogel structure (Fig. 2H) with uniformly distributed Ag NPs (Fig. 2I), confirming the successful integration of Ag NPs into the hydrogel. Silver nanoparticles (Fig. 2I) appeared as discrete, high-density regions, well-dispersed throughout the matrix. Their overlap with sulphur-rich domains supports efficient plasmonic hot-electron transfer to the conductive polymer network.

TGA was conducted to study the thermal stability of the PAM hydrogel, PAM–1% PEDOT:PSS hydrogel, and PAM–1% PEDOT:PSS–10% Ag hydrogel, as presented in Fig. 2(J–L). In the PAM hydrogel analysis (Fig. 2J), the weight loss up to 200 °C was 48.3%, corresponding to the dehydration of water.[61,62] Degradation in the range of 200–335 °C corresponds to the breaking of amide (–NH$_2$) groups, causing a 22.34% weight loss. The third zone, from 335 °C to 525 °C, corresponds to the breakdown of the polyacrylamide backbone, resulting in a 17.15% weight loss.[63,64]

A similar degradation trend is observed in the PAM–1% PEDOT:PSS hydrogel (Fig. 2K). Dehydration up to 200 °C results in a higher weight loss of 53.98% because PEDOT:PSS is hydrophilic, retaining more water. The degradation of –NH$_2$ groups occurs between 200 °C and 337 °C with a slightly reduced weight loss of 20.97%, while backbone decomposition from 337 °C up to 500 °C accounts for 16.92% weight loss. These shifts indicate slight thermal modifications induced by the incorporation of PEDOT:PSS.[65] While in the PAM–1% PEDOT:PSS–10% Ag hydrogel, the initial weight loss was 50.27% until 186 °C. This weight loss is attributed to the higher hydrophilic characteristics and silver nanoparticle doping. The degradation between 186 °C and 343 °C, with 22.79% weight loss, was due to the amide group. The final degradation occurred between 343 °C and 505 °C with 18.19% weight loss.

The presence of plasmonic Ag NPs not only influences the thermal decomposition process but also aids in the production of hot electrons, which can be readily injected into the PEDOT:PSS matrix. In conclusion, these interactions enhance charge mobility and the dynamics of the polymer chain, which, in turn, influence the decomposition temperature and thermal stability.[66,67]

2.3. Mechanical, strain and stability characteristics of plasmon-driven hot electron dynamics mediating the PAM–PEDOT:PSS–Ag hydrogel

This section provides detailed insights into the mechanical, adhesive, strain, and stability characteristics of the PAM, PAM–PEDOT:PSS, and PAM–PEDOT:PSS–Ag hydrogels, which are crucial for long-term physiological monitoring.

The mechanical characterisation of the PAM, PAM–PEDOT:PSS, and PAM–PEDOT:PSS–Ag hydrogels was tested using an Instron 5942 micro tester. Fig. 3A, B and Fig. S6 depict the stress–strain behaviour of hydrogel samples with corresponding values of S1 (PAM) 938.5 ± 17.81%, 147.9112 ± 2.7 kPa, S2 (PAM–0.5% PEDOT:PSS) 1410.8959 ± 52.31382%, 147.6785 ± 7.10911 kPa, S3 (PAM–1% PEDOT:PSS) 1542.9 ± 25.79%, 170.7033 ± 2.9182 kPa, S4 (PAM–3% PEDOT:PSS) 1466.00373 ± 82.90698%, 148.79303 ± 10.75447 kPa, S5 (PAM–1% PEDOT:PSS–5% Ag) 1758.439 ± 75.18171, 225.4853 ± 14.08 kPa, S6 (PAM–1% PEDOT:PSS–10% Ag) 2196.5 ± 70.107%, 270.082 ± 3.27628 kPa, and S7 (PAM–1% PEDOT:PSS–20% Ag) 1500.904 ± 41.41%, 188.234 ± 6.8394 kPa hydrogel compositions. The statistical analysis of the stress–strain characteristics, showing that the PAM hydrogel S1 at baseline exhibited a tensile strain of about 938.5 ± 17.81% and a tensile stress of 147.91 ± kPa, while the addition of 0.5% 1% and 3% v/v PEDOT:PSS in the S2, S3 and S4 samples significantly improved the mechanical properties, due to enhanced interactions between the polymer chains and increased conductivity due to PEDOT.

Further enhancement was made possible by introducing Ag NPs at different concentrations relative to PEDOT:PSS. At 5% (S5),
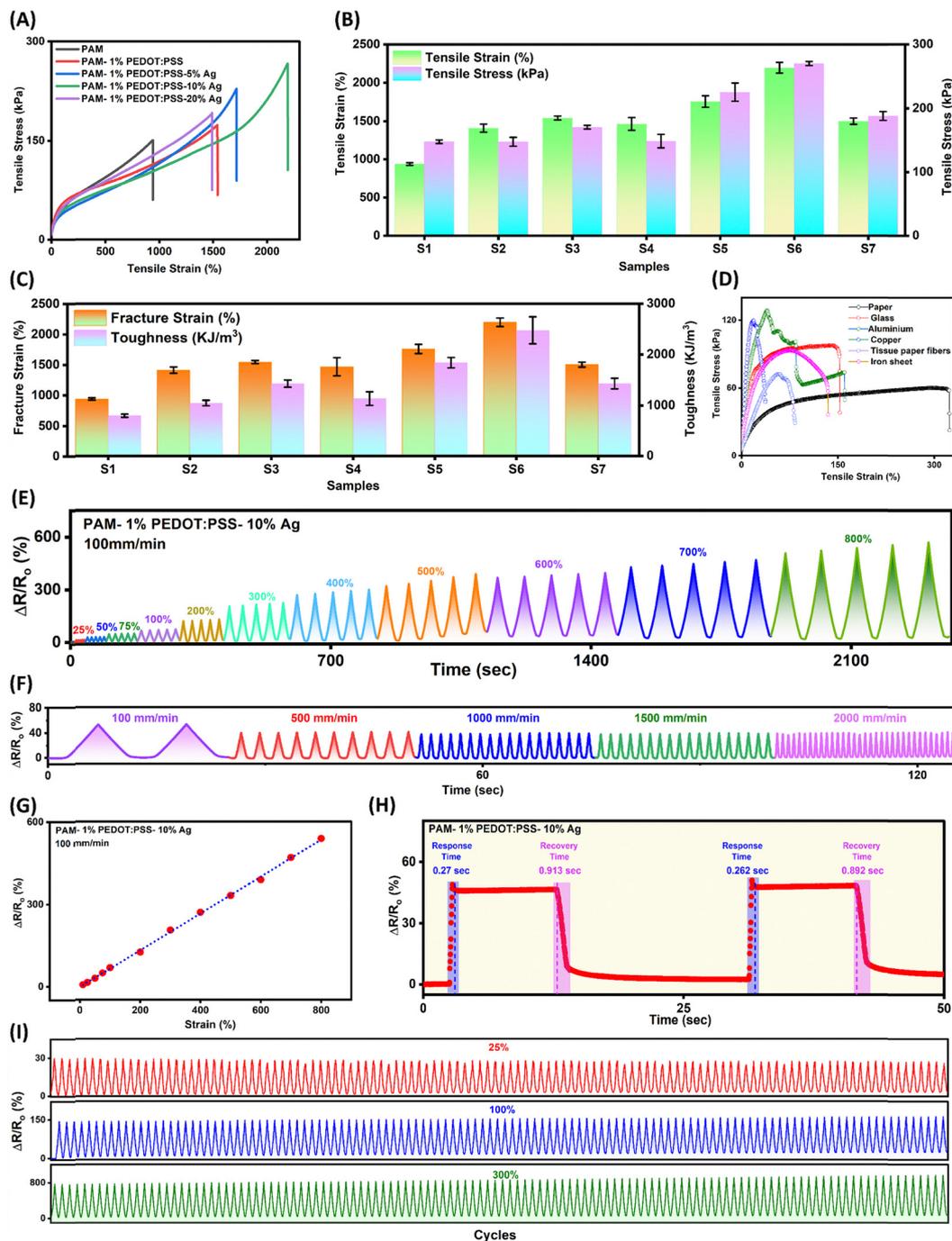
This journal is © The Royal Society of Chemistry 2026

J. Mater. Chem. B, 2026, 14, 5408–5427 | 5413

Fig. 3 Mechanical performance of PAM, PAM–PEDOT:PSS and PAM–PEDOT:PSS–Ag hydrogels, followed by adhesion and strain performance of the PAM–1% PEDOT:PSS–10% Ag hydrogel. (A and B) Stress–strain curves of hydrogel samples with corresponding values of S1 (PAM) 938.5 ± 17.81%, 147.9112 ± 2.7 kPa, S2 (PAM–0.5% PEDOT:PSS) 1410.8959 ± 52.31382%, 147.6785 ± 7.10911 kPa, S3 (PAM–1% PEDOT:PSS) 1542.9 ± 25.79%, 170.7033 ± 2.9182 kPa, S4 (PAM–3% PEDOT:PSS) 1466.00373 ± 82.90698%, 148.79303 ± 10.75447 kPa, S5 (PAM–1% PEDOT:PSS–5% Ag) 1758.439 ± 75.18171, 225.4853 ± 14.08 kPa, S6 (PAM–1% PEDOT:PSS–10% Ag) 2196.5 ± 70.107%, 270.082 ± 3.27628 kPa, and S7 (PAM–1% PEDOT:PSS–20% Ag) 1500.904 ± 41.41%, 188.234 ± 6.8394 kPa hydrogel. Each group was tested thrice ($n = 3$). (C) Fracture strain and toughness analysis of hydrogel samples with corresponding values of S1 (PAM) 938.5 ± 17.81%, 800.47 ± 32.02 KJ m^{-3}, S2 (PAM–0.5% PEDOT:PSS) 1410.8959 ± 52.31382%, 1048.11746 ± 53.62146 KJ m^{-3}, S3 (PAM–1% PEDOT:PSS) 1542.9 ± 25.79%, 1426.77 ± 70.30114 KJ m^{-3}, S4 (PAM–3% PEDOT:PSS) 1466.00373 ± 82.90698%, 1133.17089 ± 131.26255 KJ m^{-3}, S5 (PAM–1% PEDOT:PSS–5% Ag) 1758.439 ± 75.18171, 1838.672 ± 102 KJ m^{-3}, S6 (PAM–1% PEDOT:PSS–10% Ag) 2196.5 ± 70.107%, 2477.142 ± 267 KJ m^{-3}, and S7 (PAM–1% PEDOT:PSS–20% Ag) 1500.904 ± 41.41%, 1428.195 ± 104.3502 KJ m^{-3}. Each group was tested thrice ($n = 3$). (D) Stress–strain curves showing adhesion strengths of the PAM–1% PEDOT:PSS–10% Ag hydrogel to various substrates, including paper (~57.9 kPa), glass (~97.5 kPa), aluminium (~128.5 kPa), copper (~119.7 kPa), tissue paper (~59.2 kPa), and iron (~93.2 kPa), highlighting favourable adhesion properties. (E) Relative resistance changes ($\Delta R/R_0$ %) in the PAM–1% PEDOT:PSS–10% Ag hydrogel over a 25–800% strain range at 100 mm min^{-1} strain rate. (F) Relative resistance changes ($\Delta R/R_0$ %) in the PAM–1% PEDOT:PSS–10% Ag hydrogel over a 100% strain at the rates of 100 mm min^{-1}, 500 mm min^{-1}, 1000 mm min^{-1}, 1500 mm min^{-1} and 2000 mm min^{-1}. (G) Gauge factors and linear regression analysis of the PAM–1% PEDOT:PSS–10% Ag hydrogel over a 25–800% strain range at a 100 mm min^{-1} strain rate. (H) Response and recovery time of the PAM–1% PEDOT:PSS–10% Ag hydrogel at a strain rate of 100%. (I) 100 repeated stretching/releasing cycles of the PAM–1% PEDOT:PSS–10% Ag hydrogel at 25%, 100%, and 300% strains.

Paper

10% (S6), and 20% (S7), w/v Ag NP, the hydrogel reached a tensile strain and stress of 1758.4 ± 75.18%, 225.49 ± 14.08 kPa, 2196.5 ± 70.11% 270.08 ± 3.28 kPa, and 1500.9 ± 41.41%, 188.23 ± 6.84 kPa. The S6 (PAM–1% PEDOT:PSS–10% Ag) sample demonstrated peak performance, due to an optimised concentration, with plasmon-driven hot-electron dynamics enhancing polymer cross-linking and charge mobility.

Fig. 3C illustrates the fracture strain and toughness of hydrogel samples with corresponding values of S1 (PAM) 938.5 ± 17.81%, 800.47 ± 32.02 KJ m^{-3}, S2 (PAM–0.5% PEDOT:PSS) 1410.8959 ± 52.31382%, 1048.11746 ± 53.62146 KJ m^{-3}, S3 (PAM–1% PEDOT:PSS) 1542.9 ± 25.79%, 1426.77 ± 70.30114 KJ m^{-3}, S4 (PAM–3% PEDOT:PSS) 1466.00373 ± 82.90698%, 1133.17089 ± 131.26255 KJ m^{-3}, S5 (PAM–1% PEDOT:PSS–5% Ag) 1758.439 ± 75.18171, 1838.672 ± 102 KJ m^{-3}, S6 (PAM–1% PEDOT:PSS–10% Ag) 2196.5 ± 70.107%, 2477.142 ± 267 KJ m^{-3}, and S7 (PAM–1% PEDOT:PSS–20% Ag) 1500.904 ± 41.41%, 1428.195 ± 104.3502 KJ m^{-3}. The fracture strain is the maximum strain a material can withstand before failure during stretching, and toughness is the ability of hydrogels to resist fracture by dissipating large amounts of mechanical energy before failing. From the above analysis, the samples, S6 (PAM–1% PEDOT:PSS–10% Ag), demonstrated the highest fracture strain (∼2196.5 ± 70.11%) and the highest toughness (∼2477.142 ± 267 KJ m^{-3}), indicating a highly stable hydrogel with ultra-stretchability.

Fig. S7 shows the cyclic strain test of the PAM–1% PEDOT:PSS–10% Ag hydrogel at deformations of 25%, 50%, 75%, 100%, 150%, and 300%. Very low hysteresis is observed in each stretching cycle, with excellent elastic recovery, demonstrating its reliable mechanical reversibility and resilience. The adhesion performance of the PAM–1% PEDOT:PSS–10% Ag hydrogel was assessed using lap-shear tests, as shown in Fig. S8A and Fig. 3D. The adhesion strengths of the PAM–1% PEDOT:PSS–10% Ag hydrogel were analysed on various substrates, including paper (∼57.9 kPa), glass (∼97.5 kPa), aluminium (∼128.5 kPa), copper (∼119.7 kPa), tissue paper (∼59.2 kPa), and iron (∼93.2 kPa).

Moreover, Fig. S8B(a–j) visually shows the adhesiveness of the hydrogel to various substrates, which include copper (a), iron (b), tissue paper (c), aluminium (d), glass (e), foot scale (f), tweezers (g), and the human hand from different angles (h–j). The results of the experiment show the strong adhesion of the PAM–1% PEDOT:PSS–10% Ag hydrogel to various substrates, demonstrating its effectiveness for real-time physiological signal detection, particularly in dynamic environments such as continuous ECG monitoring and biomechanical motion.

The conductive hydrogels with low strain ensure stable skin contact, thereby providing a noise-free ECG signal even in dynamic environments. The comfort, toughness, and consistency of the conductive hydrogels make them ideal for long-term wearability.[68] Thorough mechanical and electrical measurements were performed to investigate the strain-sensing properties of the PAM–1% PEDOT:PSS–10% Ag hydrogel, as depicted in Fig. 3E–I.

The strain measurements at a rate of 100 mm min^{-1} over the range of 25% to 800% strain showed a steady, linearly increasing relative resistance, $\Delta R/R_0$ (%), as depicted in Fig. 3E. The PAM–1% PEDOT:PSS–10% Ag hydrogel also showed sharper $\Delta R/R_0$ (%) transitions and higher repeatability at a faster rate of 500 mm min^{-1}, as shown in Fig. S9A and B. While Fig. S10 shows that the sensitivity of the PAM–1% PEDOT:PSS–10% Ag hydrogel increased linearly from 25% to 300% at a gauge factor of ∼0.6–0.7 and increased sharply from 300% to 500% at a gauge factor of ∼1–1.2, indicating the dynamic adaptability of the sensor.

These stable strain properties are attributed to the structural design of the PAM–1% PEDOT:PSS–10% Ag hydrogel and to the plasmon-driven hot-electron dynamics introduced by Ag nanoparticles. Under mechanical deformation, localised surface plasmon resonance (LSPR) in Ag NPs generates hot electrons that facilitate charge transfer and modulate the conductive network, thereby amplifying the hydrogel's electromechanical response.[69,70] So, the PAM–1% PEDOT:PSS–10% Ag hydrogel was tested at different strain rates of 100 mm min^{-1}, 500 mm min^{-1}, 1000 mm min^{-1}, 1500 mm min^{-1} and 2000 mm min^{-1} at 100% strain, showing a stable response across all strain rates as highlighted in Fig. 3F.

The PAM–1% PEDOT:PSS–10% Ag hydrogels demonstrated predictive strain behaviour, as evidenced by linear regression ($R^2 \approx 0.99$) at 100 mm min^{-1}, with a stable, linearly increasing relative resistance $\Delta R/R_0$ (Fig. 3G). The response (∼0.27 s) and recovery (∼0.9 s) times (Fig. 3H) of the PAM–1% PEDOT:PSS–10% Ag hydrogel were investigated to highlight its sensitivity, a crucial factor for ECG wearable electrodes in dynamic monitoring. In addition, Fig. 3I and Fig. S11 demonstrate the ultrastability of the PAM–1% PEDOT:PSS–10% Ag hydrogel by applying 100 cycles of stretching and releasing at different strain levels (25%, 50%, 75%, 100%, 150%, and 300%).

In conclusion, the rapid response and recovery time, combined with ultrastability, underscore the suitability of the hydrogel for continuous, high-fidelity wearable health monitoring powered by plasmonic spatial smooth heating enhancement.

Moreover, Fig. S12A illustrates the temperature-dependent plasmonic strain-sensing behaviour of the PAM–1% PEDOT:PSS–10% Ag hydrogel under cyclic 100% strain at −20 °C, 2 °C, room temperature (∼25 °C), and 40 °C. At −20 °C, $\Delta R/R_0$ peaks (∼35%) due to a rigid, glassy state, causing microcrack formation. At 2 °C, $\Delta R/R_0$ slightly drops (∼32%) as limited chain mobility restricts crack formation. At room temperature and 40 °C, plasticization enables reversible micro-gap dynamics, enhancing conductivity and strain response, with $\Delta R/R_0$ peaks of ∼45% and ∼70%, respectively. The hydrogel showed excellent stability over 100 cycles across all temperatures (Fig. S12B).

To assess multifunctionality, circuit-based conductivity tests (Fig. S13) were conducted. The intact hydrogel completed an LED circuit (Fig. S13A). Cutting disrupted conductivity (Fig. S13B), but self-healing restored it (Fig. S13C). Stretchability was demonstrated by sustained LED illumination under strain (Fig. S13D), highlighting self-healing conductive paths that enhance mechanical stability and promise continuous cardiovascular monitoring.

This journal is © The Royal Society of Chemistry 2026

J. Mater. Chem. B, 2026, **14**, 5408–5427 | **5415**

2.4. Electrochemical, antibacterial and bio-compatibility characteristics of plasmon-driven hot electron dynamics mediating PAM–PEDOT:PSS–Ag hydrogels

This section presents the electrochemical properties, electrical conductivity, and real-time interfacial impedance of the PAM–1% PEDOT:PSS–10% Ag hydrogel in contact with skin, followed by an evaluation of its biocompatibility and antibacterial properties, key factors for long-term cardiovascular monitoring.

Electrochemical properties of PAM–1% PEDOT:PSS and PAM–1% PEDOT:PSS–10% Ag hydrogels were assessed using a three-electrode setup. Samples were immersed in phosphate-buffered saline (PBS) and placed on the working electrode. A platinum electrode served as the counter electrode, and Ag/AgCl was the reference electrode. Cyclic voltammetry (CV) was performed over a potential range of −0.5 V to 0.5 V at 25 mV s^{-1}, 50 mV s^{-1}, 75 mV s^{-1}, and 100 mV s^{-1} scan rates as highlighted in Fig. 4A, B and Fig. S14A and B.

Across all scan rates, including 25 mV s^{-1} (Fig. 4A), 50 mV s^{-1} (Fig. S14A), and 75 mV s^{-1} (Fig. S14B), and 100 mV s^{-1} (Fig. 4B), PAM–1% PEDOT:PSS and PAM–1% PEDOT:PSS–10% Ag electrodes exhibited stability and the same trend of CV. However, PAM–1% PEDOT:PSS–10% Ag demonstrated the broader, more rectangular CV loops and higher current densities, indicating superior capacitive behaviour and electron transfer. Even at a low scan rate of 25 mV s^{-1} (Fig. 4A), the PAM–1% PEDOT:PSS–10% Ag electrodes maintained stable, well-defined loops, reflecting excellent electrochemical reversibility and charge retention. These improvements are attributed to silver nanoparticles' increased surface area and conductivity, which enable efficient double-layer formation and rapid charge–discharge cycles.[71] Ag NP incorporation significantly boosts the hydrogel's capacitance, stability, and current response, making PAM–1% PEDOT:PSS–10% Ag a strong candidate for wearable bioelectronics, especially in long-term cardiovascular monitoring.

Fig. 4C illustrates the conductivity testing of four hydrogel formulations, S1 (PAM–0.5% PEDOT:PSS), S2 (PAM–1% PEDOT:PSS), S3 (PAM–3% PEDOT:PSS), and S4 (PAM–1% PEDOT:PSS–10% Ag), demonstrating the higher conductivity with increment of PEDOT:PSS concentration. The conductivity increased with PEDOT:PSS concentration from approximately 87.88 ± 2.36 mS m^{-1} in S1 (PAM–0.5% PEDOT:PSS), to 189.9 ± 2.8 mS m^{-1} in S3 (PAM–3% PEDOT:PSS), due to increased formation of connected conductive pathways in the hydrogels. However, excessive doping at 3% reduced hydrogel stretchability (Fig. 3A and B) and made S2 (PAM–1% PEDOT:PSS) 180.45 ± 6.00 mS m^{-1} the optimal base for silver nanoparticle integration.

The maximum conductivity, ∼328.82 ± 1.78 mS m^{-1}, was achieved in the PAM–1% PEDOT:PSS–10% Ag due to the synergistic effect of PEDOT:PSS and Ag nanoparticles, which improved electron mobility and reduced charge-transfer resistance.[72] These findings further reinforce the notion that selecting the polymer concentration and nanoparticle weight is a delicate balance in order to optimise the hydrogel for wearable bioelectronics in cardiovascular monitoring, where stable and efficient signal transmission is crucial.

Electrode-skin contact impedance is one of the most critical factors for non-invasive, long-term ECG-monitoring bio-electrodes. Fig. 4(D and E) and Fig. S15(A and B) illustrate the impedance and phase angle response of PAM–1% PEDOT:PSS and PAM–1% PEDOT:PSS–10% Ag hydrogel electrodes in the range of 1–100 kHz with 50 mV of bias voltage to assess the conductivity mechanism at the interface with the skin.

The PAM–1% PEDOT:PSS (Fig. 4D) demonstrated ∼205.928 kΩ, ∼6.529 kΩ, ∼1.443 kΩ, and ∼0.915 kΩ impedance at 1 Hz, 1 kHz, 10 kHz, and 100 kHz, while in comparison, PAM–1% PEDOT:PSS–10% Ag electrodes (Fig. 4E) exhibited ∼106.933 kΩ, ∼6.059 kΩ, ∼1.027 kΩ, and ∼0.548 kΩ impedance at 1 Hz, 1 kHz, 10 kHz, and 100 kHz. This reduction in impedance is attributed to the enhanced electrical conductivity and reduced interfacial resistance introduced by the plasmon enhanced hot electrons dynamics of silver nanoparticles.[72]

Fig. S15A illustrates the phase angle measurements of PAM–1% PEDOT:PSS–Ag 10% hydrogel electrodes in contact with skin across frequencies from 1 Hz to 100 kHz, showing values of −3.535°, −72.561°, −46.518°, and −15.359° at 1 Hz, 1 kHz, 10 kHz, and 100 kHz, respectively. In comparison, PAM–1% PEDOT:PSS electrodes (Fig. S15 B) exhibited −5.739°, −70.152°, −35.358°, and −12.642° at the same frequencies. The PAM–1% PEDOT:PSS–Ag 10% hydrogel electrodes showed lower phase angles at low frequencies, indicating improved charge transfer and conductivity.[73] Both electrodes demonstrated strong capacitive behaviour near 1 kHz, ideal for the acquisition of bioelectrical signals.[74] At higher frequencies, phase angles decreased, reflecting a shift toward resistive behaviour. The Ag-enhanced electrodes maintained more stable and capacitive characteristics across the spectrum, suggesting enhanced interface dynamics.[67]

The incorporation of silver nanoparticles improves conductivity, decreases interfacial resistance, and stabilizes phase behaviour, which are all critical for accurate signal acquisition in ECG. Thus, PAM–1% PEDOT:PSS–10% Ag hydrogels exhibit superior performance for next-generation wearable bioelectronics.

Biocompatibility is a crucial factor for wearable electrodes in long-term cardiovascular monitoring. So, Fig. 4(F–H) and Fig. S16 demonstrate the biocompatibility characteristics of the PAM–1% PEDOT:PSS–10% Ag hydrogel. Specifically, Fig. 4F depicts an increase in optical density on days 2 and 3, reflecting high metabolic activity and cell proliferation, as confirmed by statistical analysis ($p < 0.001$). These findings were corroborated by fluorescence microscopy, where most of the cells in Fig. 4H were green, indicating live cells, and very few were red, representing dead cells, with a uniform cell distribution and maintained cell density within the hydrogel matrix, demonstrating the excellent cytocompatibility of the hydrogel and supporting cell viability with further cell proliferation and metabolic function. Compared to the control, as presented in Fig. S16, the PAM–1% PEDOT:PSS–10% Ag electrodes showed stable cell viabilities in the range of 83–89% over three days, as depicted in Fig. 4H.

Additionally, the PAM–1% PEDOT:PSS–10% Ag hydrogel demonstrated high antibacterial properties, with a 4000-fold reduction in bacterial viability, as shown in Fig. 4I. The visual
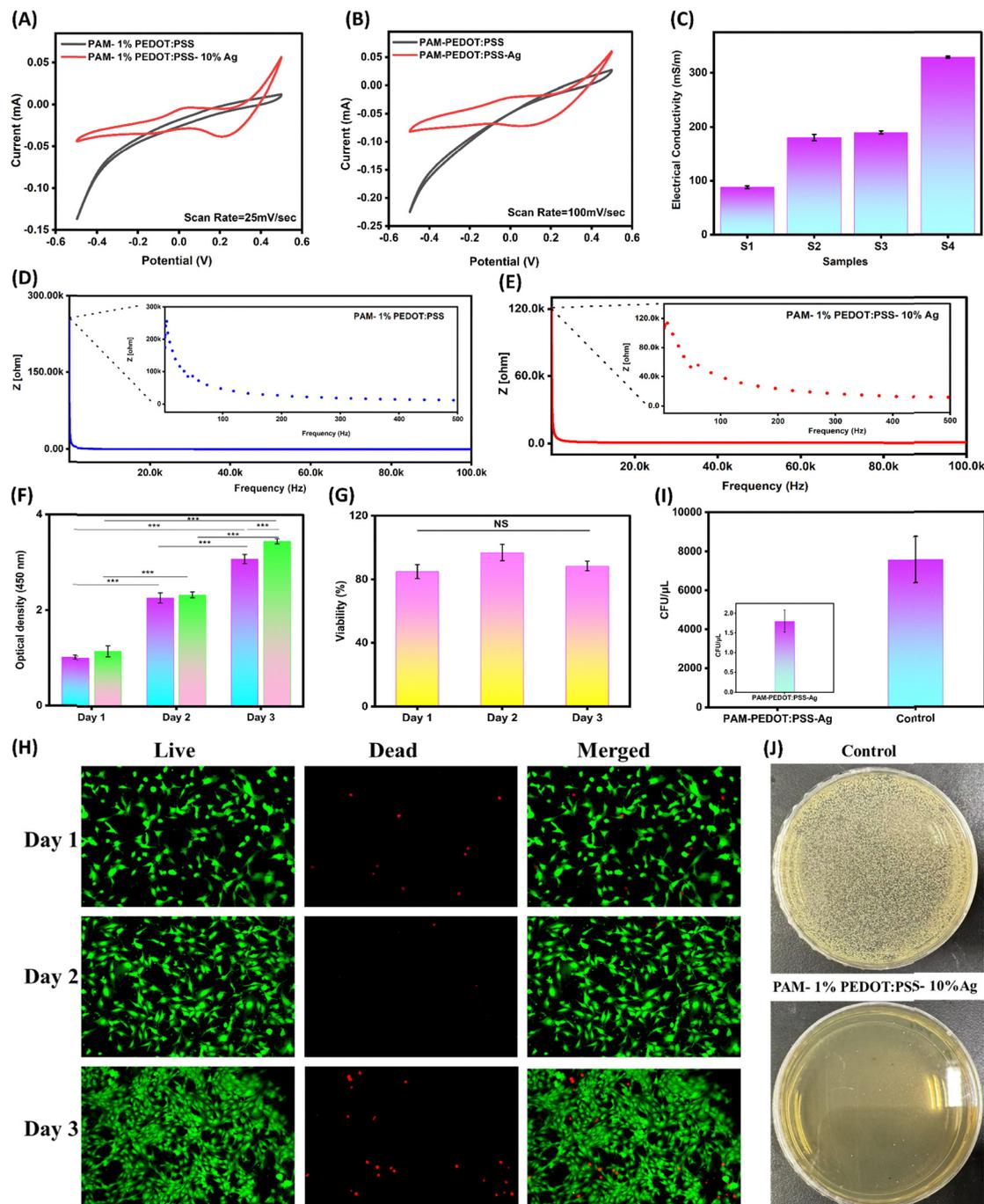
5416 | *J. Mater. Chem. B*, 2026, **14**, 5408–5427

This journal is © The Royal Society of Chemistry 2026

Fig. 4 Electrochemical, biocompatibility and antibacterial characteristics of the plasmon-driven hot electron dynamics mediating PAM−PEDOT:PSS−Ag hydrogel. (A) Cyclic voltammograms (CVs) of the PAM−1% PEDOT:PSS and PAM−1% PEDOT:PSS−10% Ag hydrogels at a scan rate of 25 mV s^{-1}. (B) Cyclic voltammograms (CVs) of the PAM−1% PEDOT:PSS and PAM−1% PEDOT:PSS−10% Ag hydrogels at a scan rate of 100 mV s^{-1}. (C) Electrical conductivity measurements for the hydrogel samples: S1 (PAM−0.5% PEDOT:PSS), S2 (PAM−1% PEDOT:PSS), S3 (PAM−3% PEDOT:PSS), and S4 (PAM−1% PEDOT:PSS−10% Ag). Each group was tested thrice ($n = 3$). (D) Electrode skin impedance measurement of the PAM−1% PEDOT:PSS hydrogel from 1 Hz to 100K Hz. (E) Electrode skin impedance measurement of the PAM−1% PEDOT:PSS−10% Ag hydrogel from 1 Hz to 100K Hz. (F) The optical density graph of the PAM for the 1% PEDOT:PSS−10% Ag hydrogel over 3 days. (H) Cell viability of the PAM−1% PEDOT:PSS−10% Ag hydrogel over 3 days. (G) Fluorescence cell viability of the PAM−1% PEDOT:PSS−10% Ag hydrogel over 3 days. (I) Quantitative analysis of bacterial growth showing significantly reduced colony-forming units (CFU µL^{-1}) in the PAM−1% PEDOT:PSS−10% Ag sample compared to the control. (J) Representative petri dish images illustrating bacterial colony density: the control shows extensive growth, while the PAM−1% PEDOT:PSS−10% Ag sample exhibits minimal colony formation, confirming its antibacterial efficacy.

This journal is © The Royal Society of Chemistry 2026

J. Mater. Chem. B, 2026, **14**, 5408−5427 | **5417**

inspection of petri dishes is presented in Fig. 4J. The control plates showed abundant bacterial colonies, whereas the PAM–1% PEDOT:PSS–10% Ag hydrogel-treated plates appeared almost clear, with only scattered colonies, due to the synergistic effect of PAM, PEDOT:PSS, and silver nanoparticles.

Overall, the combination of high electrochemical performance, excellent biocompatibility, and potent antimicrobial activity positions the PAM–1% PEDOT:PSS–10% Ag hydrogel as a highly effective electrode for AI-enabled long-term cardiovascular monitoring.

2.5. Molecular dynamics analysis of plasmon-driven hot electron dynamics mediating PAM–PEDOT:PSS–Ag hydrogels

Molecular dynamics (MD) simulations were performed on complex hydrogel systems to model the real-time environment of reactions and to understand the plasmonic effects on hot-electron dynamics. The hot-electron dynamics were simulated under different temperatures (30 °C, 50 °C, and 80 °C) in PAM PEDOT:PSS–Ag hydrogel systems.

Fig. 5A, D, and G illustrate a complex hydrogel system at 30 °C, 50 °C, and 80 °C, comprising PAM, water, glycerol, PEDOT:PSS, and silver nanoparticles. The positions of Ag nanoparticles were strategically placed near PEDOT:PSS chains to better understand plasmonically enhanced hot-electronics dynamics.

The radial distribution function (RDF) in MD analysis is a key structural function used to understand the interactions among atoms in molecules or composites. Fig. 5B, E, and H illustrate the RDF of silver nanoparticles in PAM, water, glycerol, and PEDOT:PSS, a complex system, demonstrating a linear relationship between inter-bonding peak intensity and temperature. Initially, the peak intensity was 2.66 at 30 °C, increasing to 3.85 at 50 °C and 4.37 at 80 °C.

The linear increase indicates the generation of hot electrons due to the plasmonic properties of silver nanoparticles at high temperatures.[75] Moreover, at higher temperatures, the RDF peaks broaden, indicating enhanced molecular mobility and validating the generation of hot electrons and spatially smooth heating throughout the system.[76–78]

Fig. S17A–C illustrate the detailed investigation of RDF plots for silver nanoparticles with nitrogen of PAM (PAM (Ag NPs_PAM_N)), which clearly indicates efficient charge transfer, with peak intensities of 2.19 (30 °C), 2.12 (50 °C), and 1.97 (80 °C), respectively.[79] In contrast, Fig. 5C, F, and I illustrate the interaction of Ag NPs with PEDOT:PSS (AgNPs_PEDOT:PSS), which clearly shows exponential growth in conductivity with a percolation network, especially at 80 °C.[80]

Furthermore, structural integrity and flexibility of the polymer backbone were also indicated by the presence of inter-bonding ($\sim$1.3 Å) and intra-bonding ($\sim$0.4 Å) signals at all temperatures, as demonstrated in Fig. 5J, K and Fig. S17D, respectively. This data also indicates a credible activation mechanism for a plasmonic temperature-dependent activation mechanism:[76] whereby, at 30 °C, a stable interface between Ag NPs and polymer is indicated to be biocompatible for charge transfer, at 50 °C, an increase in efficiency of plasmonic

activation balances hot electron production,[81] and at 80 °C, maximum efficiency of plasmonic activation was demonstrated to result in maximum hot electrons and structural stability.[75] In addition, Fig. 5L illustrates the atom colour coding from the MD simulation models.

In a mechanistic perspective, the difference between inter-bonding (blue) and intra-bonding (red) signals helps elucidate the mechanism of plasmon-induced charge delocalisation, leading to increased conductivity.[79,81] Conversely, intra-bonding stability[82] is responsible for greater than 2000% polymer flexibility and stretchability. Quantitative analysis indicated a conductivity of $\sim$328.82 $\pm$ 1.78 mS m^{-1} for Ag NPs_PEDOT:PSS, a fast gelation time of 420 s, and Ag$^+$ release with antibacterial efficacy $\geq$99.7%. These results confirm the plasmonic hot-electron mechanism and provide the groundwork for designing next-generation bioelectronic materials.

2.6. Application of the plasmon-driven hot electron dynamics mediating PAM–PEDOT:PSS–Ag hydrogel for real-time electrocardiography (ECG) signals and biomechanical signals

The plasmon-driven hot-electron dynamics mediating PAM–1% PEDOT:PSS–10% Ag hydrogel electrodes were characterized by exceptional sensitivity, flexibility, enhanced conductivity, antibacterial activity, and high biocompatibility, thereby enabling real-time monitoring of ECG and biomechanical signals across different parts of the human body.

We evaluated the applicability of the plasmon-driven hot-electron dynamics mediating PAM–1% PEDOT:PSS–10% Ag hydrogel for monitoring ECG signals, as illustrated in Fig. 6. We affixed the PAM–1% PEDOT:PSS–10% Ag hydrogel electrodes to the left and right wrists, and a ground electrode to the right ankle for ECG recording, as shown in Fig. 6A. The acquired ECG signals exhibited distinct P–Q–R–S–T wave patterns, with an SNR of 25.47 dB, capturing all the standard features characteristic of clinical ECGs. Additionally, to confirm the compatibility of the PAM–1% PEDOT:PSS–10%Ag hydrogel electrodes on different anatomical sites, electrodes were affixed to the chest region (Fig. 6B), demonstrating ECG signals with an SNR of 24.03 dB. The ECG signals from both anatomical sites consistently contain high-SNR peaks, outperforming those from commercial electrodes.

In high-SNR environments, long-term monitoring is crucial for wearable ECG electrodes. Therefore, we monitored the ECG signal from the PAM–1% PEDOT:PSS–10% Ag electrode on the 1st, 3rd, and 7th days (Fig. 6C). The electrodes exhibit reliable performance, with only a slight decline in SNR from 23.85 to 21.84 dB, demonstrating exceptional stability and accuracy for long-term cardiovascular monitoring.

The reliability and accuracy of the developed PAM–1% PEDOT:PSS–10% Ag hydrogel electrodes were further validated against a reference signal, as depicted in Fig. 6D. Simultaneous blood pressure recordings were obtained at rest and during exercise using a commercial CNAP blood pressure monitoring system. During exercise, physiological stress is induced, elevating blood pressure. In parallel, the PAM–1% PEDOT:PSS–10%Ag hydrogel electrodes clearly monitored the dynamics of
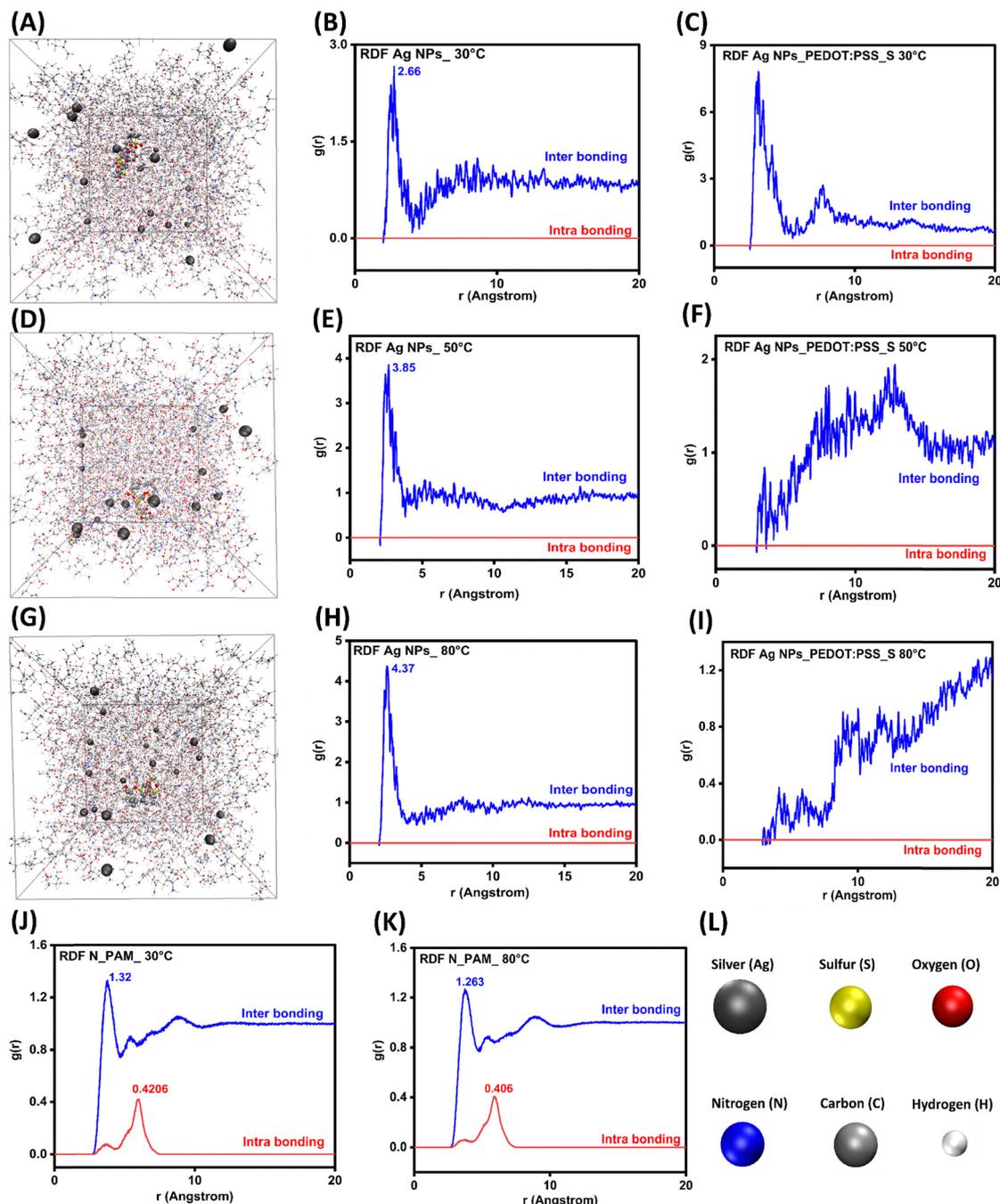
5418 | *J. Mater. Chem. B*, 2026, **14**, 5408–5427

This journal is © The Royal Society of Chemistry 2026

Fig. 5 Molecular dynamics simulations of the plasmon-driven hot electron dynamics mediating PAM−PEDOT:PSS−Ag hydrogel. (A) Molecular dynamic simulation model of the PAM−1% PEDOT:PSS−10% Ag hydrogel at 30 °C, (B) the radial density function (RDF) plot of the Ag-NPs at 30 °C, (C) the radial density function (RDF) plot of Ag-NPs-PEDOT:PSS_S at 30 °C, (D) the molecular dynamic simulation model of the PAM−1% PEDOT:PSS−10% Ag hydrogel at 50 °C, (E) the radial density function (RDF) plot of the Ag-NPs at 50 °C, (F) the radial density function (RDF) plot of Ag-NPs−PEDOT:PSS_S at 50 °C, (G) the molecular dynamic simulation model of the PAM−1% PEDOT:PSS−10% Ag hydrogel at 80 °C, (H) the radial density function (RDF) plot of Ag-NPs at 80 °C, (I) theradial density function (RDF) plot of Ag-NPs−PEDOT:PSS_S at 80 °C, (J) the radial density function (RDF) plot of N_PAM at 30 °C, (K) the radial density function (RDF) plot of N_PAM at 80 °C, and (L) the colour coding of atoms used in the MD simulations.

the cardiovascular event, as evidenced by increased heart rate and shortened R–R intervals. The mean blood pressures during exercise and rest were 95/130 mmHg and 80/110 mmHg, respectively, showing the real-time monitoring capability of the developed hydrogel toward changing cardiovascular states.

The findings confirm that the hydrogel can perform continuous, accurate monitoring across various physiological conditions.

The PAM−1% PEDOT:PSS−10% Ag electrodes were also used in the rodent model to assess signal acquisition accuracy at high heart rates. Rodents' heart rates are six times higher than those of
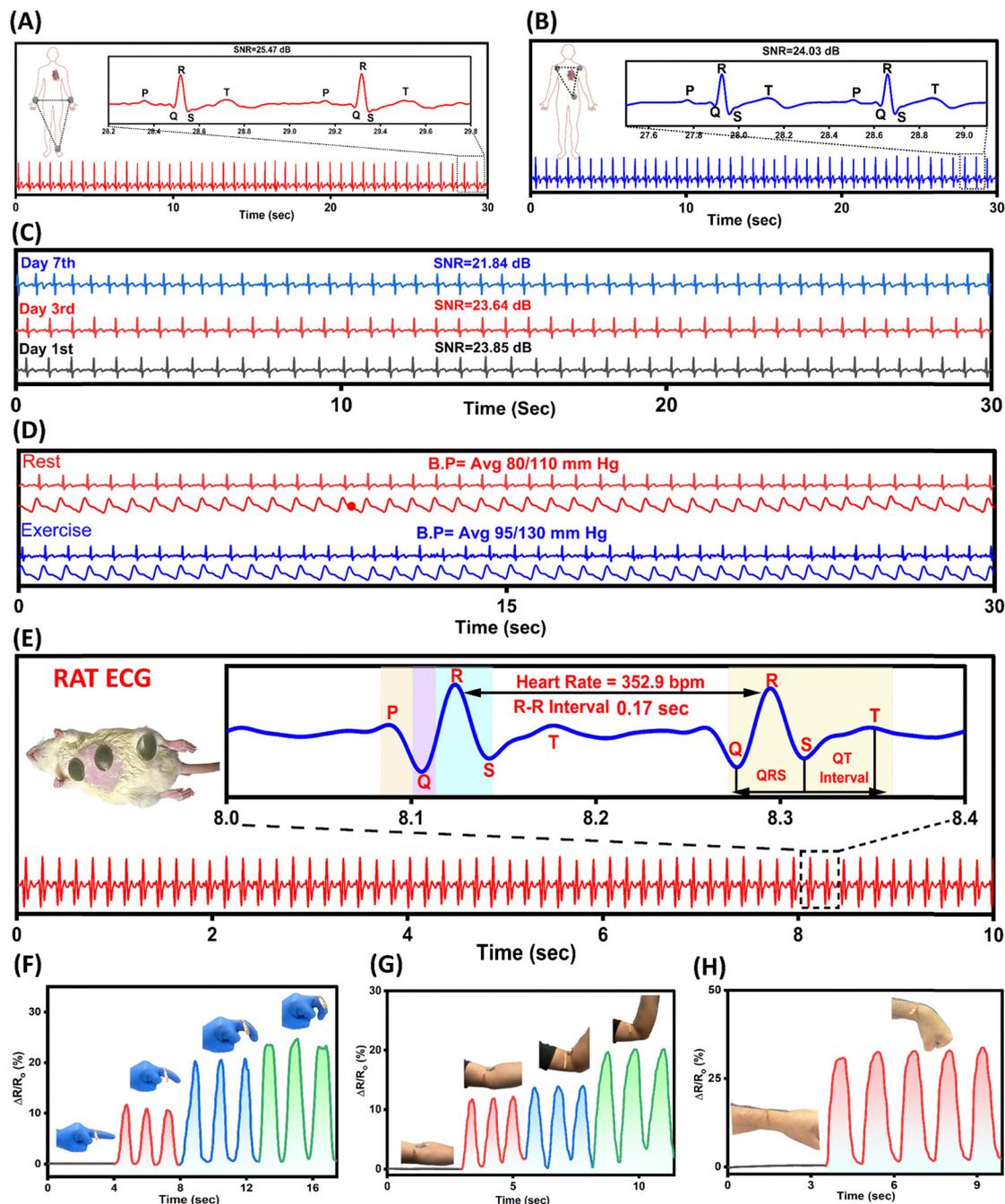
This journal is © The Royal Society of Chemistry 2026

J. Mater. Chem. B, 2026, **14**, 5408–5427 | **5419**

Fig. 6 Plasmon-driven hot electron dynamics mediating the PAM–1% PEDOT:PSS–10% Ag hydrogel for real-time ECG and biomechanical signal monitoring. (A) A high-resolution human ECG signal recorded from the hand region, clearly displaying standard PQRST peaks. (B) A high-resolution human ECG signal was recorded from the chest region, and distinct PQRST peaks were also shown. (C) Long-term human ECG monitoring using the PAM−1% PEDOT:PSS−10% Ag electrodes on days 1, 3, and 7, demonstrating electrode stability through signal-to-noise ratio (SNR) analysis. (D) Human ECG monitoring during rest and exercise conditions, with reference blood pressure signals, validating the accuracy and reliability of the PAM−1% PEDOT:PSS−10% Ag electrodes. (E) High-resolution rat ECG signal showing standard PQRST peaks, with an R–R interval of 0.17 seconds and a heart rate of 352.9 bpm. (F) Real-time monitoring of relative resistance changes ($\Delta R/R_0$) in PAM−1% PEDOT:PSS−10% Ag electrodes during finger bending at various angles. (G) Real-time monitoring of relative resistance changes ($\Delta R/R_0$) during elbow bending at multiple angles. (H) Real-time monitoring of relative resistance changes ($\Delta R/R_0$) during wrist bending at various angles.

humans. Fig. 6E shows the ECG signal acquisition in the rodent model. High-resolution ECG signals with all the features were observed. The bpm was calculated using the R-R interval formula to investigate the high heart rate. The bpm was 352.9, with an R–R interval of 0.17 seconds. In conclusion, these results further confirm the translational potential of the PAM–1% PEDOT:PSS–10% Ag hydrogel electrode for preclinical use and its suitability for high-performance biopotential monitoring in small-animal models.

5420 | *J. Mater. Chem. B*, 2026, **14**, 5408–5427

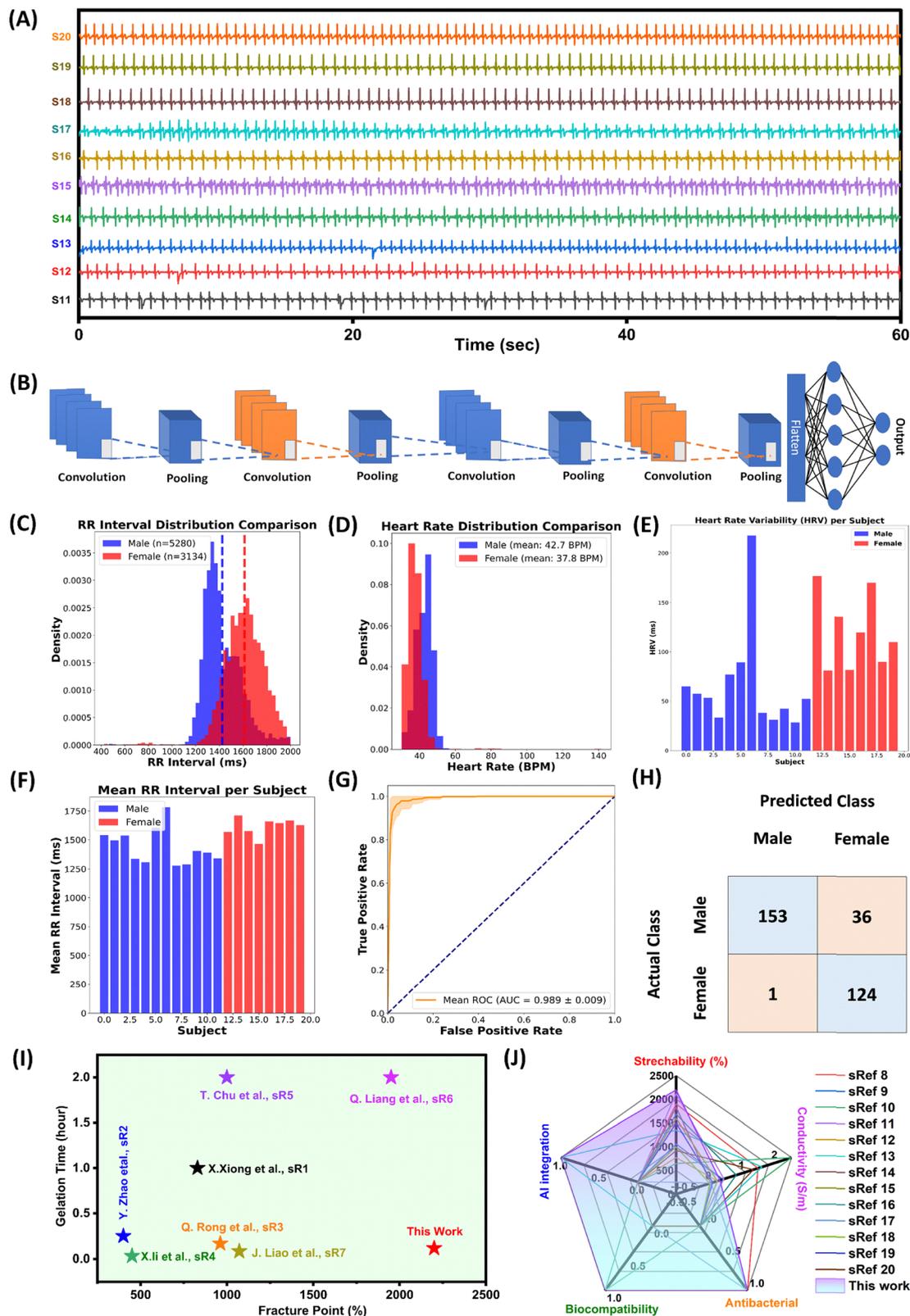This journal is © The Royal Society of Chemistry 2026

Fig. 7 AI-enabled ECG-based gender classification for enhanced cardiovascular monitoring. (A) ECG data from 11–20 subjects were used for model training and testing. (B) A convolutional neural network (CNN) architecture is designed for ECG-based gender classification. (C) Comparison of R–R interval distributions across 20 subjects. (D) Heart rate distribution showing males averaging 42.7 BPM and females 37.8 BPM. (E) Subject-wise heart rate variability (HRV) comparison between male and female groups. (F) Mean R–R interval per subject for male and female ECG data. (G) Receiver operating characteristic (ROC) curve illustrating CNN model performance. (H) Confusion matrix summarising CNN classification results. (I) Comparative graph showing gelation time *versus* fracture point for references in the SI (sR1–sR7), emphasising differences in mechanical performance. (J) Benchmark comparison of the developed PAM−1% PEDOT:PSS−10% Ag hydrogel against literature data from references in the SI (sR8–sR20).

This journal is © The Royal Society of Chemistry 2026

J. Mater. Chem. B, 2026, **14**, 5408–5427 | **5421**

Following high-resolution biopotential monitoring, biomechanical motion was investigated to demonstrate the practical reliability of the PAM–1% PEDOT:PSS–10% Ag hydrogel electrodes. The wearable sensor was developed from a PAM–1% PEDOT:PSS–10% Ag hydrogel and positioned at different body joints to monitor strain as it changed with motion. Fig. 6F illustrates the finger joint motion with various angles from $0°$ to $90°$, followed by the hinge joint (Fig. 6G) bending, wrist joint bending (Fig. 6H), and patella (Kneecap) joint (Fig. S18) in the same angular range. The change in resistance responses during angular bending of all joints was consistent and stable, confirming the mechanical adaptability of the hydrogel sensor.

2.7. AI-enabled ECG-based gender classification for enhanced cardiovascular monitoring using the plasmon-driven hot electron dynamics mediating PAM–PEDOT:PSS–Ag hydrogel

ECG-based gender classification is an exciting concept for improving cardiovascular monitoring and personalised care. Features such as QRS duration, QT interval, heart rate, and T-wave morphology differ by gender and have the potential to improve diagnostic accuracy further, thereby enhancing risk prediction.[83] The integration of AI models with ECG data revolutionises wearable CVD diagnostic systems, enabling high-accuracy gender classification. Generally, females are at higher risk of CVDs compared to males, so gender based ECG morphology can be a promising biometric for early prediction of CVDs.[84]

The ECG signals were collected using a plasmon-driven hot electron dynamics mediating PAM–1% PEDOT:PSS–10% Ag hydrogel to conduct gender classification tasks to advance cardiovascular monitoring systems. The dataset consisted of 20 subjects (12 males and 8 females, respectively), as shown in Fig. 7A and Fig. S19, and in Table S2.

Each ECG signal was sampled at 2000 Hz for 5 minutes, then down-sampled to 125 Hz, and finally divided into nonoverlapping segments of 512 samples each to improve computational efficiency and model generalisation. This type of segmentation ensured that each sample was statistically independent; it also enhanced sample size and the generalisation of the proposed model, thereby reducing overfitting. A 1-D CNN model was proposed with four consecutive CNN blocks, each with filter sizes of 32, 64, 128, and 256, and kernel sizes of 7, 5, 3, and 3, respectively. This ensured that local and global features were extracted from the input ECG signals to capture gender-related cardiac patterns, as shown in Fig. 7B. The model was implemented using the Adam optimiser with a learning rate of 0.001 and a batch size of 64, and its performance was evaluated using 5-fold cross-validation.

Physiological validation of this model includes a range of ECG-related parameters. The distribution of RR intervals, as shown in Fig. 7C, and the distribution of heart rate is shown in Fig. 7D, where the averages are 42.7 BPM for males and 37.8 BPM for females, with a statistically significant difference between the genders.

Fig. 7E shows that males exhibit HRV, consistent with gender differences in autonomic regulation. The mean RR intervals for

Table 1 5-Fold cross-validation performance

5-Fold cross validation	Accuracy	F1 score	Precision	Recall
Fold 1	0.9618	0.9620	0.9651	0.9618
Fold 2	0.9172	0.9180	0.9315	0.9172
Fold 3	0.9554	0.9557	0.9599	0.9554
Fold 4	0.9936	0.9936	0.9937	0.9936
Fold 5	0.9840	0.9841	0.9846	0.9840
Average	0.9624	0.9627	0.9670	0.9624

each individual, as shown in Fig. 7F, also validate this model's robustness, as gender differences are evident for each individual.

Fig. 7G shows the ROC curve, which indicates this model's high classification accuracy. The curve is more towards the top-left corner, and there is less variance across all folds. Additionally, Fig. 7H shows the confusion matrix, indicating that this model's classification is asymmetric. The model's performance on a five-fold cross-validation is listed in Table 1. The model's validation is quite strong, and its accuracy is high. These attributes support potential use in cardiovascular risk assessment, personalised medicine, clinical ECG interpretation, and biometric authentication.

To assess the multifunctional performances of the plasmon-driven hot electron dynamics mediating PAM–1% PEDOT:PSS–10%Ag hydrogel, a comparative analysis was made against prior state-of-the-art hydrogels reported in high-impact journals.

Fig. 7I and Table S3 present the relationship between gelation time and mechanical stretchability (fracture point). The hydrogel developed in this work exhibits the highest fracture point ($\sim$2200%) and the shortest gelation time ($\sim$0.1167 h), compared to the studies reported in the references in the SI (sR1–sR7). These results could confirm the hydrogel's ultrafast gelation and ultrahigh stretchability, making it highly suitable for real-time and wearable applications. Furthermore, Fig. 7J and Table S4 present a radar chart comparing the multifunctional performance of five key parameters: stretchability, conductivity, antibacterial properties, biocompatibility, and AI integration. The hydrogel developed in this study demonstrated excellent performance in terms of stretchability, conductivity, antibacterial properties, and AI integration, while maintaining good biocompatibility, as depicted by the shaded purple region. Conversely, most of these references in the SI (sR8–sR20) also presented a degree of trade-off, wherein highly conductive materials also tended to have either poor mechanical properties or limited AI capabilities. The highly integrated material properties reported in these references suggest that the PAM–1% PEDOT:PSS–10%Ag hydrogel is a promising material for future AI-enabled cardiovascular monitoring systems.

3. Conclusion

In summary, we report a plasmon-driven conductive PAM–PEDOT:PSS–Ag hydrogel that is ultra-stretchable, highly conductive, mechanically robust, antibacterial, biocompatible, and capable of recording a high-quality ECG signal for long-term monitoring. The hydrogels demonstrated strain-adaptive

5422 | *J. Mater. Chem. B*, 2026, **14**, 5408–5427

This journal is © The Royal Society of Chemistry 2026

properties with high adhesiveness, allowing them to firmly attach to the substrate and eliminate susceptibility to motion artefacts, thereby preventing the hydrogel from falling off under ECG-wearing conditions. The simulation studies, including MD and DFT analyses, validated the plasmonic hot-electronic dynamics and demonstrated enhanced molecular interactions. The ECG application was investigated in animal models and in humans. Additionally, to advance wearable ECG technology, a machine learning model was used to analyse the data for predictive demographic analytics. All these results underscore the great potential of hydrogels for next-generation personalised cardiovascular monitoring and bioelectronics.

4. Materials & methodology

4.1. Materials acquisition

Acrylamide (AM, A800656), N,N'-methylene bis-acrylamide (MBAA, N813086), and silver nano-powder (60–120 nm, S8179570) were obtained from Macklin. Ammonium persulfate (APS, A112448) and PEDOT:PSS (1.5%, CAS 155090-83-8) were purchased from Aladdin. Glycerol (G8190) was sourced from Solarbio.

The NIH-3T3 fibroblast cell line was obtained from the ATCC. The cells were maintained in a culture medium consisting of Dulbecco's Modified Eagle's Medium (DMEM) (Gibco, #11875085, USA) supplemented with 10% fetal bovine serum (FBS) (Gibco, #10270106, USA) and 1% penicillin–streptomycin (Gibco, #15140122, USA). The culture medium was changed every two days. The cells were incubated at 37 °C in a humidified incubator with 5% CO_2. The cells were subcultured at 80% confluence.

4.2. Hydrogel preparation

A measured quantity of Ag NPs dispersed in water was sonicated using a probe sonicator for 30 minutes. Subsequently, specific amounts of acrylamide (AM), N,N'-methylenebisacrylamide (MBAA), and ammonium persulfate (APS) were added to achieve the desired hydrogel formulation (Table S1). The mixture was then exposed to focused UV light at a distance of 5 cm under RTP, initiating crosslinking and completing hydrogel formation within 420 seconds. Experiments were conducted multiple times to validate the fast gelation with ultrastability.

4.3. Characterization

4.3.1. Morphological, material, mechanical, electrochemical and strain testing. Morphological analysis was performed using an environmental scanning electron microscope (ESEM, Philips XL30) operated at 10 kV in low-vacuum mode to prevent material degradation.

Surface chemical composition was examined *via* X-ray photoelectron spectroscopy (XPS) using a Thermo Scientific K-Alpha system. Samples were mounted on conductive carbon tape and placed on a standard XPS holder. Survey scans were conducted at 200 eV, while high-resolution scans were performed at 20 eV.

Fourier-transform infrared (FTIR) spectroscopy was performed on a PerkinElmer spectrometer in transmission mode, scanning from 400 to 4000 cm^{-1} at a resolution of 4 cm^{-1}.

Thermal properties were assessed using a PerkinElmer DSC 8000 differential scanning calorimeter. Measurements were taken over a temperature range of 120 to 800 °C at a heating rate of 20 °C min^{-1}.

Mechanical and strain properties were assessed using an Instron 5942 micro tester. The samples were measured to be 50 mm × 10 mm × 1–2 mm and were subjected to stress–strain, cyclic strain, compression, cyclic compression, leap shear adhesive and various strain rates during testing, with resistance measurements conducted using a Keithley DAQ6510 system. The rate of change of relative resistance[85] is defined as

$$\frac{\Delta R}{R_0} (\%) = \left(\frac{R - R_0}{R_0} \right) \times 100$$

where R and R_0 are the final and initial resistance values of the PAM–1% PEDOT:PSS–10% Ag hydrogel during strain application, respectively.

Toughness was quantified as the area under the stress–strain curve, calculated through numerical integration. Each measurement was repeated at least three times to ensure reproducibility and statistical reliability.

The strain gauge factor (GF)[89] is calculated as:

$$GF = ((\Delta R - R_0)/\varepsilon) \times 100$$

where ε represents the strain.

The electrical conductivity of the hydrogels was determined using a two-point probe method. The dimensions were verified with a Vernier calliper and a screw micrometre. The conductivity formula[86] used was:

$$\sigma = l/R \times A$$

where σ is the conductivity, l is the length of the hydrogel samples, A represents the hydrogel area (thickness and width), and R is the measured resistance.

To analyse the strain-responsive characteristics of the PAM–1% PEDOT:PSS–10% Ag hydrogel at different temperatures, the samples were prepared and stored at four temperatures: −20 °C, 2 °C, room temperature (around 25 °C), and 40 °C. Each hydrogel was kept at the designated temperature for 24 hours to ensure uniform temperature throughout the sample. The samples were then subjected to mechanical testing on an Instron 5942 microtester, while electrical measurements were performed using a Keithley DAQ6510 data acquisition system. The hydrogel samples were cycled with tensile strain up to 100% and the relative resistance change ($\Delta R/R_0$) was continuously recorded to study the temperature-dependent electromechanical behaviour.

A simple LED circuit was used to demonstrate the hydrogel's visual conductivity. The PAM–1% PEDOT:PSS–10% Ag hydrogel was inserted between two copper electrodes connected to a 5 V power supply and an LED. The hydrogel switched on the LED, switched off after cutting the hydrogel, and switched on again

This journal is © The Royal Society of Chemistry 2026

J. Mater. Chem. B, 2026, **14**, 5408–5427 | 5423

after self-healing, verifying the restoration of conductivity. The LED was continuously switched on while the hydrogel was stretched.

The hydrogel samples were soaked in PBS, then placed in contact with the working electrode for electrochemical characterisation. For the counter electrode, a platinum electrode was used, while an Ag/AgCl reference electrode was used as the reference electrode. For the electrochemical characterisation, cyclic voltammetry (CV) was conducted over a range of voltages from -0.5 V to 0.5 V, with scan rates of 25, 50, 75, and 100 mV s^{-1}.

The impedance of the skin electrode was measured with a HIOKI IM3590 chemical impedance analyser. The two electrodes, each 1.5 mm thick and attached to the hand at RTP, were separated by 4 cm. The measurement was carried out in the frequency range from 1 Hz to 100 kHz with an AC bias voltage of 50 mV.

4.3.2. Biocompatibility and antibacterial testing. The PAM–1% PEDOT:PSS–10% Ag hydrogel samples were subjected to a multi-step process: first, they were dipped in a 75% ethanol solution overnight, then rinsed with PBS to obtain purified samples, and finally exposed to UV light to obtain completely sterilised samples. The extraction medium was prepared by transferring the sterilised hydrogels into Dulbecco's Modified Eagle's Medium (DMEM) and incubating for 24 hours at 4 °C. The filtrate obtained was filtered through a 0.2 μm filter and stored at 4 °C for future use. This entire procedure was conducted in accordance with the standard GB/T 16886.12/ISO 10993-12.

As for the NIH-3T3 cells, they were plated at a density of 2×10^3 cells per mL in 100 μL of DMEM in 96-well plates. The next day, the medium was replaced with the 100 μL prepared hydrogel extract. Cell viability was assessed using the Cell Counting Kit-8 (CCK-8) on days 1, 2, and 3. The absorbance at 450 nm was determined.

Live/dead cell staining was performed at every time point with 5 μM Calcein AM (Invitrogen, #C3100MP, USA) at 37 °C for 20 minutes, followed by 5 μM propidium iodide (PI) (Sigma-Aldrich, #81845, USA) at room temperature for 1 minute. The fluorescent images were obtained using a Nikon Eclipse Ci microscope (Japan) and analysed with ImageJ software (NIH, USA). The results were represented as mean ± standard deviation from three independent trials. The differences among the groups were analysed using Student's t-test. The following conditions were considered for statistical significance: $p < 0.01$ (), $p < 0.001$ (), $p < 0.0001$ (), and NS = not significant.

Pseudomonas aeruginosa PAO1 and *Staphylococcus aureus* 15 981 were cultured overnight at 37 °C in 2 mL of Luria-Bertani (LB) medium (Becton, Dickinson and Company, #244620, USA), reaching bacterial concentrations of approximately $\approx 10^9$ CFU mL^{-1}. PAM–1% PEDOT:PSS–10% Ag samples (dimensions: $10 \times 10 \times 1$ mm^3) were immersed in 500 μL of phosphate-buffered saline (PBS) for antibacterial testing. Subsequently, 5 μL of the bacterial suspension was added to each sample, which was incubated at 37 °C for 24 hours.

After incubation, the solution from each sample was collected and diluted in sequence. The diluted samples were plated on LB agar to determine colony-forming units (CFUs). The bacterial count was calculated using the formula:

$$\text{CFU per mL} = (\text{colonies} \times \text{dilution factor})/\text{volume plated (mL)}$$

4.3.3. Theoretical and computational details. Geometry optimisations were performed using density functional theory (DFT) with the B3LYP hybrid functional to obtain relaxed molecular structures, as implemented in the Gaussian09 package. The 6-31G(d,p) basis set was used for C, H, O, and S atoms, whereas the LANL2DZ basis set, along with its effective core potential, was used for silver (Ag).[87] This enabled proper treatment of the transition-metal portion of the PEDOT:PSS complex.[88] Non-covalent interactions (NCIs) were also studied using the Reduced Density Gradient (RDG) method on the DFT-optimised structures of PAM, glycerol, and the PSS/PEDOT complex. This was done using the Multiwfn package.[25] The resulting data were visualised using VMD, which is included in the SI.

A supercell was created to mimic the conductive hydrogel model with Ag nanoparticles, PEDOT:PSS, glycerol, PAM, and water molecules. The supercell consisted of 17 Ag nanoparticles, 398 glycerol molecules, 298 PAM molecules, and 497 water molecules that were distributed around the PEDOT:PSS structure. The system was enclosed in a cubic box with a side length of 60 Å, which corresponds to a box size of $60 \times 60 \times 60$ Å^3. Molecular dynamics simulations were performed at constant temperatures of 303 K, 323 K, and 353 K at a fixed pressure of 1 GPa. The simulations were conducted at a constant temperature, using periodic boundary conditions and the minimum-image convention, as described in a previous study.[89]

van der Waals interactions were modelled using a 12.5 Å cutoff, while long-range electrostatic interactions were treated *via* the Ewald summation method. Integration was performed using the velocity Verlet algorithm with a 1 fs time step. All MD simulations used the CHARMM force field and were performed with GROMACS.[90]

4.3.4. Application acquisition. The application and ECG data were recorded using a continuous blood pressure monitoring device and a computer-based data acquisition system (NIBP100D, BIOPAC Systems Inc.). Data collection from all 20 subjects was conducted in accordance with the Human Ethics guidelines of the Hong Kong Science Park (Reference number: HKSTP:2023-005). Informed consent was obtained from each subject before data collection. The individuals depicted in the figures – B.K. and I.G. – have given their permission for publication of their images.

For the rat ECG study, 20 male Sprague-Dawley (SD) rats, aged 4–6 weeks and weighing 200–335 g, were used. The rats were provided by the Laboratory Animal Services Centre (LASEC) of the Chinese University of Hong Kong (CUHK). The experimental procedures were conducted according to institutional and governmental ethical guidelines, with approval from the Animal Research Ethics Committees of the City University of Hong Kong (CityU) and the Chinese University of Hong Kong

5424 | *J. Mater. Chem. B*, 2026, **14**, 5408–5427

This journal is © The Royal Society of Chemistry 2026

(CUHK), as well as the Department of Health of the Hong Kong Special Administrative Region (HKSAR).

The rats were housed in pairs in standard polycarbonate cages to avoid stress from isolation while still allowing management of the experimental conditions. The housing was provided by the LARU (Laboratory Animal Research Unit) of City University (CityU). It was done under very strictly controlled environmental conditions: 25 ± 1 °C, 60–70% humidity, and a 12 hour light/dark cycle (lights on at 07:00, off at 19:00) so that the animals could synchronise with their natural circadian rhythms. Throughout the experimental period, all animals were allowed to consume as much standard laboratory rodent chow (commercial pellet diet) as they wanted and filtered drinking water to ensure proper nutrition and hydration.

4.3.5. AI-data description. Gender identification is categorised as an auxiliary biometric technology which extracts demographic features of individuals. This technology is, in fact, a crucial part of the process that allows human beings to communicate with computer systems. The importance of gender recognition is that it reflects different behavioural traits and social characteristics that males and females have. In this experiment, ECG signals taken from our device were utilized. Of the 20 subjects, 12 were men, and 8 were women. Each signal was sampled at 2000 Hz and lasted 5 minutes.

4.3.6. AI-data pre-processing. Initially, for model training, the ECG signals were down-sampled from 2000 Hz to 125 Hz as a preprocessing step to train the CNN model faster and improve generalisation. The use of this technique for down-sampling significantly reduced the input feature space, thereby reducing computational complexity and memory requirements during forward and backwards propagation. The ECG signals were then sliced into non-overlapping segments of 512 samples each for model training and evaluation. This segmentation technique achieves several crucial objectives in deep learning-based gender classification.

To start with, the non-overlapping fixed window length of 512 samples, covering 2 seconds, is sufficient to capture the entire heartbeat and its morphological changes. Yet, it is still manageable computationally for the CNN architecture. Because of the non-overlapping segmentation method, the training samples were statistically independent of each other, which helps prevent data leakage and reduces the chance of overfitting that might occur with overlapping windows. Moreover, this segmentation technique helps expand the dataset by generating multiple independent datasets for each ECG signal, thereby increasing the model's training data volume and enabling it to learn gender-discriminating features.

4.3.7. AI model structure. In our project, a CNN model was applied for ECG-based gender classification tasks. The backbone of the network comprises four individual convolutional units, each one of them featuring a 1D convolutional layer with moderately increasing filter sizes (32, 64, 128, and 256) and shrinking kernel sizes (7, 5, 3, and 3) that allow the extraction of both local temporal patterns and broad morphological features typical of gender-related differences in heart activity. This deep learning model is excellent for the gender classification task

because it can be used to determine the most essential features in a temporal way and automatically learns them from the raw ECG signals, for instance, the morphology of the QRS complex, the heart rate variability, and the T-wave characteristics, all of which have gender-specific variations. The model is trained with a batch size of 64 samples, a learning rate of 0.001, and the Adam optimiser. At the same time, 5-fold cross-validation is applied to better assess the model's performance and generalisation across different data partitions, and to obtain more accurate estimates of classification accuracy while minimising the risk of overfitting to data subsets.

Author contributions

Conflicts of interest

There are no conflicts to declare.

Data availability

Data collected from human participants, described in Fig. 6, 7 and Fig. S18, S19, are not available for confidentiality reasons. Other experimental data supporting this article are available from the corresponding author upon request.

Supplementary information (SI) is available. See DOI: https://doi.org/10.1039/d5tb02743h.

Acknowledgements

This journal is © The Royal Society of Chemistry 2026

J. Mater. Chem. B, 2026, **14**, 5408–5427 | **5425**

University of Hong Kong, partially supported the work described in this paper.

References

1 S. Min, J. An, J. H. Lee, J. H. Kim, D. J. Joe, S. H. Eom, C. D. Yoo, H.-S. Ahn, J.-Y. Hwang and S. Xu, *Nat. Rev. Cardiol.*, 2025, 1–20.

2 B. Khan, Z. Riaz and B. L. Khoo, *Mater. Sci. Eng., R: Repo.*, 2024, **159**, 100804.

3 B. Khan, R. T. Khalid, U. Amara, N. Imdad, M. H. Masrur, M. Awais, A. Q. Laghari, B. Khan, M. Elgendi and B. L. Khoo, *J. Sci.: Adv. Mater. Devices*, 2025, 101030.

4 D. Li, T.-R. Cui, J.-H. Liu, W.-C. Shao, X. Liu, Z.-K. Chen, Z.-G. Xu, X. Li, S.-Y. Xu and Z.-Y. Xie, *Nat. Commun.*, 2025, **16**, 3259.

5 S.-H. Sunwoo, S. I. Han, C. S. Park, J. H. Kim, J. S. Georgiou, S.-P. Lee, D.-H. Kim and T. Hyeon, *Nat. Rev. Bioeng.*, 2024, **2**, 8–24.

6 N. T. Scholte, A. E. van Ravensberg, A. Shakoor, E. Boersma, E. Ronner, R. A. de Boer, J. J. Brugts, N. Bruining and R. M. van der Boon, *NPJ Dig. Med.*, 2024, **7**, 279.

7 Y. Maithani, B. Choudhuri, B. Mehta and J. Singh, *Sens. Actuators, A*, 2021, **332**, 113068.

8 Y. Lee, H. Rhee, G. Kim, W. H. Cheong, D. H. Kim, H. Song, S. N. Kay, J. Lee and K. M. Kim, *Nat. Commun.*, 2025, **16**, 1–12.

9 S. Lee, D. H. Ho, J. Jekal, S. Y. Cho, Y. J. Choi, S. Oh, Y. Y. Choi, T. Lee, K.-I. Jang and J. H. Cho, *Nat. Commun.*, 2024, **15**, 5974.

10 A. H. Umar, M. A. Othman, F. K. C. Harun and Y. Yusof, *IEEE Sens. J.*, 2021, **21**, 18353–18367.

11 Y. Zhao, S. Zhang, T. Yu, Y. Zhang, G. Ye, H. Cui, C. He, W. Jiang, Y. Zhai and C. Lu, *Nat. Commun.*, 2021, **12**, 4880.

12 F. Wang, Y. Xue, X. Chen, P. Zhang, L. Shan, Q. Duan, J. Xing, Y. Lan, B. Lu and J. Liu, *Adv. Funct. Mater.*, 2024, **34**, 2314471.

13 B. Khan, W. Khan, M. H. Masrur, R. T. Khalid, M. Awais, B. Khan, B. L. Khoo and S. Abdullah, *J. Sci.: Adv. Mater. Devices*, 2025, **10**, 100889.

14 Q. Li, B. Tian, G. Tang, H. Zhan, J. Liang, P. Guo, Q. Liu and W. Wu, *J. Mater. Chem. A*, 2024, **12**, 3589–3600.

15 H. Ding, Y. Gu, Y. Ren, C. Hu, Q. Qiu, D. Wu, J. Mou, Z. Wu and H. Zhou, *J. Mater. Chem. C*, 2024, **12**, 3030–3052.

16 B. Khan, S. Abdullah and S. Khan, *Micromachines*, 2023, **14**, 1005.

17 H. Sun, S. Wang, P. Wang, L. Bai, M. Tan, F. Yang, R. Wang and X. He, *Adv. Sci.*, 2025, **12**, e13487.

18 J. Yu, R. Wan, F. Tian, J. Cao, W. Wang, Q. Liu, H. Yang, J. Liu, X. Liu and T. Lin, *Small*, 2024, **20**, 2308778.

19 J. Yin, S. Wang, X. Xiao, F. Manshaii, K. Scott and J. Chen, *Matter*, 2025, **8**(2).

20 B. Khan, U. Amara, B. Khan, W. U. Khan, R. u S. Ahmad, M. S. Khan, M. E. Hilal and B. L. Khoo, *Adv. Sci.*, 2025, **12**, e07853.

21 J. Lee and S. H. Ko, *Nanoscale Horiz.*, 2025, **10**, 1501–1516.

22 K. Bayoumy, M. Gaber, A. Elshafeey, O. Mhaimeed, E. H. Dineen, F. A. Marvel, S. S. Martin, E. D. Muse, M. P. Turakhia and K. G. Tarakji, *Nat. Rev. Cardiol.*, 2021, **18**, 581–599.

23 S. M. Srinivasan and V. Sharma, *AI in Disease Detection: Advancements and Applications*, 2025, pp. 123–146.

24 B. Khan, R. T. Khalid, K. U. Wara, M. H. Masrur, S. Khan, W. U. Khan, U. Amara and S. Abdullah, *Chem. Eng. J.*, 2025, **505**, 159478.

25 T. Lu and F. Chen, *J. Comput. Chem.*, 2012, **33**, 580–592.

26 T. Lu, *J. Chem. Phys.*, 2024, **161**(8).

27 Z. Jing, X. Dai, X. Xian, X. Du, M. Liao, P. Hong and Y. Li, *RSC Adv.*, 2020, **10**, 23592–23606.

28 O. Nadtoka, N. Kutsevol, V. Krysa and B. Krysa, *Mol. Cryst. Liq. Cryst.*, 2018, **672**, 1–10.

29 M. Guo, Y. Wu, S. Xue, Y. Xia, X. Yang, Y. Dzenis, Z. Li, W. Lei, A. T. Smith and L. Sun, *J. Mater. Chem. A*, 2019, **7**, 25969–25977.

30 H. Yousefian, A. Babaei-Ghazvini, A. A. Isari, S. A. Hashemi, B. Acharya, A. Ghaffarkhah and M. Arjmand, *Surf. Interfaces*, 2024, **51**, 104481.

31 T. Horii, Y. Li, Y. Mori and H. Okuzaki, *Polym. J.*, 2015, **47**, 695–699.

32 Z. Cao, Z. Chen and L. Escoubas, *Opt. Mater. Express*, 2014, **4**, 2525–2534.

33 S. Devaraju, A. K. Mohanty, D.-h Won and H.-j Paik, *Mater. Adv.*, 2023, **4**, 1769–1776.

34 J. Xu, T. Cai, H. Hu, C. Meng, X. Dong, Q. Zhao and J. He, *Chem. Eng. J.*, 2024, **487**, 150671.

35 M. Zeng, J. Ding, Y. Tian, Y. Zhang, X. Liu, Z. Chen, J. Sun, C. Wu, L. Zhou and H. Yin, *Adv. Mater.*, 2025, 2505635.

36 J. Yang, J. Fan, X. Xiong, Q. Jiang, P. Li, J. Jian and L. Chen, *Appl. Phys. A*, 2024, **130**, 157.

37 J. Wang, Y. Yao, X. Hao, J. Pan, T. Zhuang, L. Guo and H. Wang, *Adv. Funct. Mater.*, 2025, 2504171.

38 H. Zhou, X. Niu, X. Ding, F. Yu and H. Yang, *J. Appl. Polym. Sci.*, 2024, **141**, e54859.

39 C. Xiong, F. Wei, W. Li, P. Liu, Y. Wu, M. Dai and J. Chen, *ACS Omega*, 2018, **3**, 10716–10724.

40 B. Gieroba, A. Sroka-Bartnicka, P. Kazimierczak, G. Kalisz, A. Lewalska-Graczyk, V. Vivcharenko, R. Nowakowski, I. S. Pieta and A. Przekora, *Int. J. Biol. Macromol.*, 2020, **159**, 911–921.

41 C. Xie, S. Yang, X. Xu, J.-W. Shi and C. Niu, *J. Nanopart. Res.*, 2020, **22**(1), 25.

42 N. Díez, A. Moyseowicz, S. Grylegicz, B. Grzyb and G. Gryglewicz, *RSC Adv.*, 2015, **5**, 81831.

43 J. Guo, K. Zhang, P. Luo, N. Wu, S. Peng, L. Wei, Y. Liu, M. He, J. Yu, S. Qin, Q. Fan, T. Luo and J. Xiao, *RSC Adv.*, 2024, **14**, 1602–1611.

44 M. Islam, H. Deb, K. Hasan, N. Khoso, M. Hossain, Y. Wentong, X. Qi, Y. Dong, Y. Zhu and Y. Fu, *J. Mater. Sci.*, 2022, **57**(32), 15451–15463.

45 H. Mori, K. Hasebe and M. Terano, *J. Mol. Catal. A: Chem.*, 1999, **140**, 165–172.

5426 | *J. Mater. Chem. B*, 2026, **14**, 5408–5427

This journal is © The Royal Society of Chemistry 2026

46 C. Li, N. Zhang and P. Gao, *Mater. Chem. Front.*, 2023, **7**, 3797–3802.

47 G. Greczynski and L. Hultman, *Prog. Mater. Sci.*, 2020, **107**, 100591.

48 N. Kruse and S. Chenakin, *Appl. Catal., A: Gen.*, 2011, **391**, 367–376.

49 S. Rafique, N. A. Roslan, S. M. Abdullah, L. Li, A. Supangat, A. Jilani and M. Iwamoto, *Org. Electron.*, 2019, **66**, 32–42.

50 S.-Y. Lien, P.-C. Lin, W.-R. Chen, C.-H. Liu, K.-W. Lee, N.-F. Wang and C.-J. Huang, *The Mechanism of PEDOT:PSS Films with Organic Additives*, 2022, **12**(8), 1109.

51 Y. Wang, Y. Hu, D. Han, Q. Yuan, T. Cao, N. Chen, D. Zhou, H. Cong and L. Feng, *Org. Electron.*, 2019, **70**, 63–70.

52 A. Al-Sarraj, K. Saoud, A. Elmel, S. Mansour and Y. Haik, *SN Appl. Sci.*, 2021, **3**(1), 15.

53 M. Salvadori, R. Ando, C. Nascimento and B. Corrêa, *J. Environ. Sci. Health, Part A*, 2017, **52**, 1–9.

54 J. Wang, G. Xia, L. Xia, Y. Chen, Q. Li, H. Zeng, W. Yang, Y. Du, W. He and Y. Chen, *J. Mater. Sci.: Mater. Electron.*, 2024, **35**, 1931.

55 J. Klein, V. de Lima, J. Feira, R. Brandalise and M. M. Forte, *J. Appl. Polym. Sci.*, 2016, **133**, 43634.

56 Z. Zheng, Q. Wu and S. Zhong, *HPW/PAM Catalyst for Oxidative Desulfurization-Synthesis, Characterization and Mechanism Study*, 2022, **10**, 402.

57 N. Nagireddy, K. Varaprasad, S. Ravindra, V. Gangireddygari, K. Reddy, K. Muniswamy Reddy and K. Raju, *Colloids Surf., A*, 2011, **385**, 20–27.

58 B. Djibrine, H. Zheng, M. Wang, S. Liu, X. Tang, S. Khan, A. Navarro Jiménez and L. Feng, *Int. J. Polym. Sci.*, 2018, 1–12.

59 P. Swpu, *Petroleum*, 2016, **2**, 399–407.

60 H. Luo, Y. Liu, H. Lu, Q. Fang and H. Rong, *ACS Omega*, 2021, **6**(9), 6240–6251.

61 L. Zerroual and I. Derafa, *J. Inorg. Organomet. Polym. Mater.*, 2020, **30**, 4544–4551.

62 S. Faridi, A. Mobinikhaledi, H. Moghanian and M. Shabanian, *BMC Chem.*, 2023, **17**, 125.

63 S. S. Mahrous, M. S. Mansy and E. Abdel Galil, *J. Radioanal. Nucl. Chem.*, 2022, **331**, 4731–4744.

64 L. Gaabour, *Results Phys.*, 2017, **7**, 2153–2158.

65 S. Hossain, Y. Yamamoto and N. Kishi, *J. Appl. Polym. Sci.*, 2024, **141**, e55713.

66 H. J. Son, H.-K. Park, J. Y. Moon, B.-K. Ju and S. H. Kim, *Sustainable Energy Fuels*, 2020, **4**, 1974–1983.

67 C. Slaughter, S. Velasco-Bosom, X. Tao, R. R.-M. Serrano, S. Kissovsky, R. Mizuta, D. Mantione, S. T. Keene, G. G. Malliaras and A. Dominguez-Alfaro, *J. Mater. Chem. C*, 2024, **12**, 14944–14954.

68 Y. Shi, X. Fu, W. Wang and D. Yu, *Colloids Surf., A*, 2023, **662**, 130998.

69 F. S. Ameer, S. Varahagiri, D. W. Benza, D. R. Willett, Y. Wen, F. Wang, G. Chumanov and J. N. Anker, *J. Phys. Chem. C*, 2016, **120**, 20886–20895.

70 F. Diehl, S. Hageneder, S. Fossati, S. K. Auer, J. Dostalek and U. Jonas, *Chem. Soc. Rev.*, 2022, **51**, 3926–3963.

71 K. Nešović, V. Kojić, K. Y. Rhee and V. Mišković-Stanković, *Corrosion*, 2017, **73**, 1437–1447.

72 R. G. Melendez, K. J. Moreno, I. Moggio, E. Arias, A. Ponce, I. Llanera and S. E. Moya.

73 N. Lopez-Larrea, S. Wustoni, M. I. Peñas, J. Uribe, A. Dominguez-Alfaro, A. Gallastegui, S. Inal and D. Mecerreyes, *Adv. Funct. Mater.*, 2024, **34**, 2403708.

74 F. Tan, X. Li, X. Li, M. Xu, K. A. Shahzad and L. Hou, *Biomolecules*, 2024, **14**, 95.

75 A. Goswami, A. S. Kim and W. Cai, *J. Appl. Phys.*, 2024, **136**, 100901.

76 T. P. Rossi, P. Erhart and M. Kuisma, *ACS Nano*, 2020, **14**, 9963–9971.

77 L. Van Turnhout, Y. Hattori, J. Meng, K. Zheng and J. Sá, *Nano Lett.*, 2020, **20**, 8220–8228.

78 Y. Hu, Y. Wang and Y. Yao, *Mater. Today Commun.*, 2023, **34**, 105292.

79 J. Khurgin, A. Y. Bykov and A. V. Zayats, *Elight*, 2024, **4**, 15.

80 S. Sarkar, A. C. Bhowal, R. Kandimalla and S. Kundu, *Synth. Met.*, 2021, **279**, 116848.

81 J. Luo, Q. Wu, L. Zhou, W. Lu, W. Yang and J. Zhu, *Photon. Insights*, 2023, **2**, R08.

82 B. G. Levine, J. E. Stone and A. Kohlmeyer, *J. Comput. Phys.*, 2011, **230**, 3556–3569.

83 N. H. Arif, M. R. Faisal, A. Farmadi, D. Nugrahadi, F. Abadi and U. A. Ahmad, *J. Electron., Electromed. Eng., Med. Informatics*, 2024, **6**, 107–115.

84 S. Desai, A. Munshi and D. Munshi, *J. Mid-Life Health*, 2021, **12**, 8–15.

85 Z. Zhou, W. Yuan and X. Xie, *Mater. Chem. Front.*, 2022, **6**, 3359–3368.

86 Y. Ohm, C. Pan, M. J. Ford, X. Huang, J. Liao and C. Majidi, *Nat. Electron.*, 2021, **4**, 185–192.

87 Y. Yang, M. N. Weaver and K. M. Merz Jr, *J. Phys. Chem. A*, 2009, **113**, 9843–9851.

88 J. E. Del Bene, W. B. Person and K. Szczepaniak, *J. Phys. Chem.*, 1995, **99**, 10705–10707.

89 B. Khan, M. Elhousseini, S. B. Ahmed, L. Lyu, H. Chen, B. Khan, I. Gunasekaran, F. Chuhan, S. LIU and Z. Yang, *Chem. Eng. J.*, 2025, **513**, 162384.

90 W. Humphrey, A. Dalke and K. Schulten, *J. Mol. Graphics*, 1996, **14**, 33–38.

This journal is © The Royal Society of Chemistry 2026

J. Mater. Chem. B, 2026, **14**, 5408–5427 | **5427**